



DETERMINATION OF CLOUD AND  
PRECIPITATION CHARACTERISTICS  
FROM SATELLITE, RADAR AND  
RAINGAGE ANALYSIS

LP-127

FINAL REPORT  
TWDB CONTRACTS NO. 14-90023 AND 14-00004

Prepared by:

DONALD R. HARAGAN  
JERRY JURICA  
COLLEEN A. LEARY  
ATMOSPHERIC SCIENCE GROUP  
TEXAS TECH UNIVERSITY  
LUBBOCK, TEXAS

Prepared for:

TEXAS DEPARTMENT OF WATER RESOURCES  
AUSTIN, TEXAS

Funded by:

DEPARTMENT OF THE INTERIOR, BUREAU OF RECLAMATION  
TEXAS DEPARTMENT OF WATER RESOURCES

June 1980

TECHNICAL REPORT STANDARD TITLE PAGE

1. REPORT NO.		2. GOVERNMENT ACCESSION NO.		3. RECIPIENT'S CATALOG NO.	
4. TITLE AND SUBTITLE  Final Report of Contract IAC (78-79)2104				5. REPORT DATE January 1, 1980	
				6. PERFORMING ORGANIZATION CODE  580/330	
7. AUTHOR(S) Donald R. Haragan Jerry Jurica Colleen A. Leary				8. PERFORMING ORGANIZATION REPORT NO. LP-127	
9. PERFORMING ORGANIZATION NAME AND ADDRESS Atmospheric Science Group Texas Tech University P.O. Box 4320 Lubbock, Texas 79409				10. WORK UNIT NO. 5540	
				11. CONTRACT OR GRANT NO. IAC (78-79) 2104	
12. SPONSORING AGENCY NAME AND ADDRESS Texas Department of Water Resources P.O. Box 13087 Capitol Station Austin, Texas 78711				13. TYPE OF REPORT AND PERIOD COVERED 1 January 1979 to 31 December 1979	
				14. SPONSORING AGENCY CODE	
15. SUPPLEMENTARY NOTES Submitted to: Office of Atmospheric Resources Management Water and Power Resources Service Denver Federal Center; Box 25007; Denver, Colorado 80225					
16. ABSTRACT  Data gathered during the Texas HIPLEX field programs of 1977, 1978 and 1979 are analyzed and discussed. Specific data treated are recording rain gauge data, digitized radar data and geostationary satellite radiance data. Individual analyses are presented as well as results derived from integration of the several data sources into a more complete case study of certain dates. It is concluded that such integration of individual analyses yields greatly improved understanding of the relevant meteorological processes.					
17. KEY WORDS AND DOCUMENT ANALYSIS a. DESCRIPTORS-- Weather modification/cumulus clouds/meteorological radar/rain gauges/geostationary satellite/rainfall/cloud seeding  b. IDENTIFIERS-- Texas/High Plains/HIPLEX  c. COSATI Field/Group COWRR:					
18. DISTRIBUTION STATEMENT Available from the National Technical Information Service, Operations Division, Springfield, Virginia 22161.				19. SECURITY CLASS (THIS REPORT) UNCLASSIFIED	
				20. SECURITY CLASS (THIS PAGE) UNCLASSIFIED	
				21. NO. OF PAGES	
				22. PRICE	

HIPLEX FINAL REPORT  
for the Period  
1 January 1979 to 31 December 1979

submitted to  
Texas Department of Water Resources  
and the  
U.S. Department of the Interior

by  
Atmospheric Science Group  
Texas Tech University

work performed under  
Contract IAC(78-79)2104  
TDWR Contract No. 14-90023

LP-127

Principal Investigators  
Donald R. Haragan  
Jerry Jurica  
Colleen A. Leary

June 1, 1980

## TABLE OF CONTENTS

Abstract	iii
List of Figures	iv
List of Tables	vi
Introduction	1
Work Performed	1
Task 1. Determination of Cloud Properties from Satellite Data	1
Task 2. Integration of Satellite Data with Raingage and Radar Measurement	16
Task 3. Rainfall Analysis	35
Task 4. Radar Data Collection for 1979 Field Experiment	53
Task 5. Support to the Field Program	68
References	69

## ABSTRACT

Data gathered during the Texas HIPLEX field programs of 1977, 1978 and 1979 are analyzed and discussed. Specific data treated are recording raingage data, digitized radar data and geostationary satellite radiance data. Individual analyses are presented as well as results derived from integration of the several data sources into a more complete case study of certain dates. It is concluded that such integration of individual analyses yields greatly improved understanding of the relevant meteorological processes.

## LIST OF FIGURES

1-1.	Location and approximate operational coverage of the two satellite data sources.	2
1-2.	The area of study.	3
1-3.	Variation of percent cloud cover with time.	7
1-4.	Curves of the frequency distribution of visible radiance values on 22 June.	8
1-5.	Curves of the frequency distribution of visible radiance values of 24 June.	9
1-6.	Curves of the frequency distribution of visible radiance values on 27 June.	10
1-7.	Curves of the frequency distribution of visible radiance values on 8 July.	11
2-1.	Surface chart at 1800 GMT and 500 mb chart at 1200 GMT on 8 July 1977.	17
2-2.	Variation of total network precipitation with time on 8 July 1977.	19
2-3.	Precipitation analysis of the total precipitation from 1800 GMT 8 July to 0000 GMT 9 July 1977.	20
2-4.	PPI displays on 8 July 1977 from the M-33 radar at Snyder.	21
2-5.	Cloud albedo, cloud top temperature and rainfall intensity on 8 July 1977.	23
2-6.	Isohyet pattern for the period 1945-2000 GMT 8 July 1977.	25
2-7.	RHI display derived from M-33 radar for the azimuth angle $235^{\circ}$ at 1942 GMT 8 July 1977, together with cloud top height derived from satellite infrared data and actual raingage measurements.	26
2-8.	Isohyet pattern for the period 2015-2030 GMT 8 July 1977.	28
2-9.	RHI display derived from M-33 radar data for the azimuth angle $253^{\circ}$ at 2018 GMT 8 July 1977, together with cloud top height derived from satellite infrared data and actual raingage measurements.	29
2-10.	Same as Figure 2-9 for azimuth angle $259^{\circ}$ .	31
2-11.	Atmospheric soundings taken at Big Spring on 8 July 1977.	33

- 3-1. GOES EAST enhanced infrared satellite photograph of the cloud pattern over the Texas HIPLEX area at 2100 GMT on 8 July 1977. 38
- 3-2. RHI (a) and low-level ( $1^{\circ}$ ) PPI (b) displays derived from Snyder digital radar data for 2104 GMT, 8 July 1977. 40
- 3-3. Temperature (solid line) and dew point (dashed line) at 2100 GMT on 8 July at Post plotted in skew T - log p format. 41
- 3-4. The 2100 GMT Post sounding from Fig. 3-3 superposed on the lower portions of Zipser's (1977, Fig. 8) collection of soundings in and beneath tropical anvil clouds associated with intense tropical convection. 41
- 3-5. Surface winds at 2100 GMT on 8 July 1977 superposed on the low-level radar echo pattern of Fig. 3-2b. 42

LIST OF TABLES

1-1.	Number of clouds of different sizes	6
1-2.	Comparison of percent cloud cover and cloud numbers from satellite radiance data and photographic imagery.	13
3-1.	HIPLEX radar characteristics Snyder, Texas 1977	36
3-2.	Wind direction (degrees) and speed ( $m s^{-1}$ ) at 2100 GMT	44
3-3.	1977 Precipitation	46
3-4.	1978 Precipitation	48
3-5.	1977 Storm Data	50
3-6.	1978 Storm Data	51
4-1.	Skywater radar Texas HIPLEX scanning modes 1979	54
4-2.	Inventory of digital radar data.	55
4-3.	Inventory of 16mm movie film	63
4-4.	Inventory of radar video tapes Summer 1979	66

## INTRODUCTION

Since its initiation, the ultimate objective of the Texas HIPLEX program has been the integration of surface, upper air, radar and satellite data in a manner beneficial to the proper design and subsequent evaluation of a rainfall enhancement experiment. The analysis effort at Texas Tech University during 1979 reflects this integrative approach. Surface rainfall, radar, and satellite data have been utilized in order to better define storm rainfall and the mesoscale convective systems responsible.

## WORK PERFORMED

Five tasks were undertaken during calendar year 1979.

### Task 1. Determination of Cloud Properties from Satellite Data

The principal responsibility of the meteorological satellite support provided to the 1979 Texas HIPLEX program by Texas Tech has been twofold: (1) the development of techniques to expand the analysis of data by utilizing satellite measurements, and (2) support of forecasting and aircraft operations during the summer field program. The data source for the effort has been visible and infrared radiance measurements and photographic imagery from the GOES (Geostationary Operational Environmental Satellite) system, utilizing both GOES-WEST and GOES-EAST data (Figure 1-1). The data analysis activity has consisted of two related portions: the determination of cloud properties from satellite data and integration of satellite data with rain-gage and radar data (Task 2). The analysis was performed by Mr. Shih-Cheng Chao, who conducted the research as a thesis project and has recently completed all requirements for the M.S. degree in Atmospheric Science. The direct support to the field program is covered under Task 5.

The accomplishments under Task 1 have been achieved through the analysis of four case study days selected from the 1977 Texas HIPLEX field season - 22, 24 and 27 June and 8 July 1977. The area of study is shown in Figure 1-2. These four days were selected because of the availability of good satellite, rain-gage and radar data sets. On two days, 8 July and 22 June, substantial rainfalls occurred; on 24 and 27 June, however, little or no precipitation was recorded within the rain-gage network. The objective in this Task was

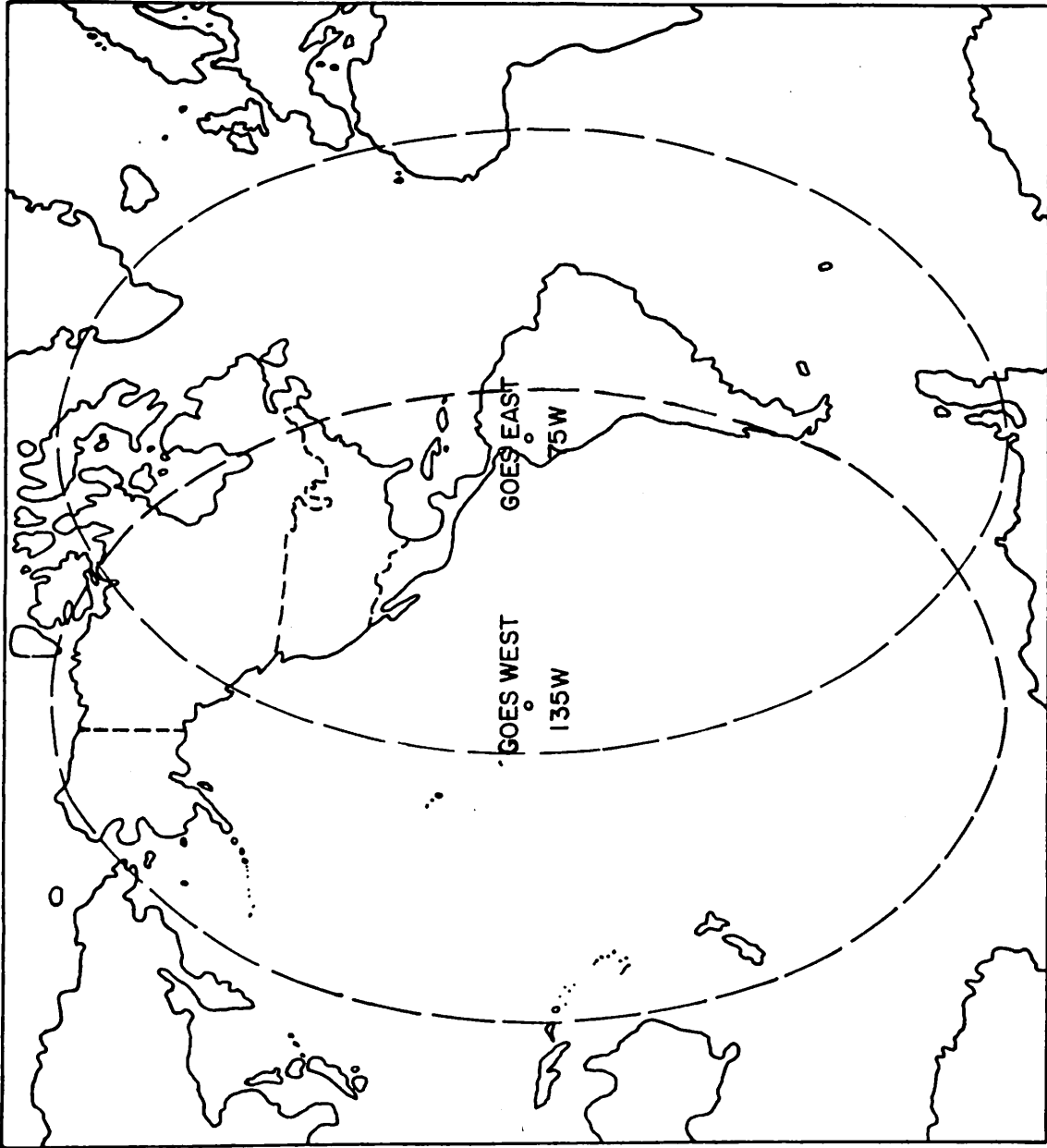


Figure 1-1 Location and approximate operational coverage of the two satellite data sources: GOES WEST at 135° W and GOES EAST at 75° W longitude.

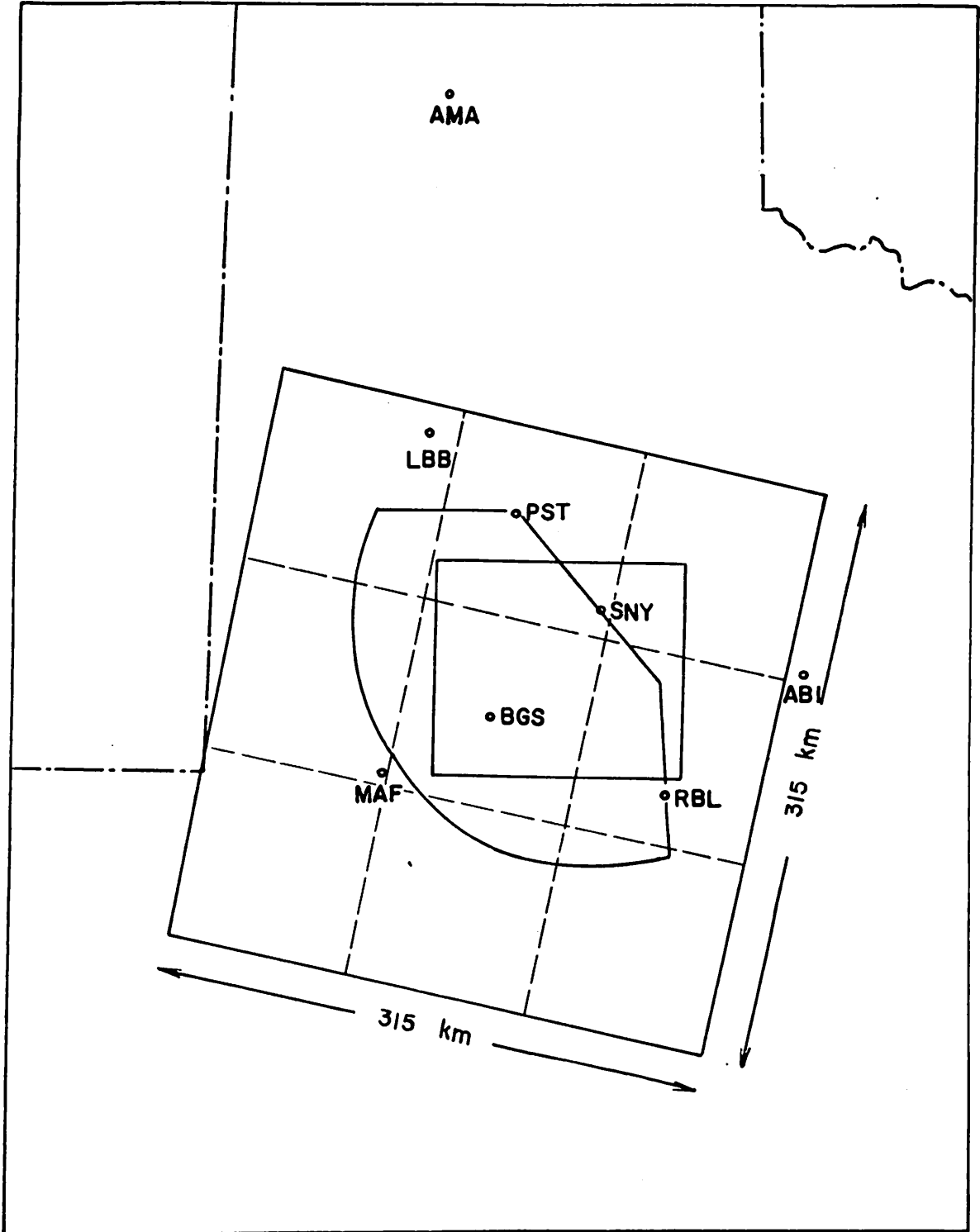


Figure 1-2 The area of study. The sector at the center is the Texas HIPLEX study region.

to derive cloud properties from the satellite data, and then compare and contrast results between rainfall and non-rainfall days.

The visible radiance data were analyzed with a cloud summary program. The principal input parameter for each time on the four case study days was the critical brightness, determined with the ADVISAR, to distinguish cloud from non-cloud surface. A number of statistical products, such as mean cloud brightness and variance of cloud brightness, as well as the cloud size were generated through the cloud summary program. After the cloud-by-cloud statistics were accumulated, the following comprehensive information was obtained: (1) percentages of cloud cover and non-cloud area within the study area; (2) mean brightness values of the total cloud and non-cloud area; (3) brightness distribution of all data points; (4) distribution of cloud mean brightness; and (5) distribution of cloud size.

The number of clouds and percent cloud cover was obtained for each time on the four case-study days. The minimum cloud size of interest in this study is a cloud of four pixels, equivalent in area to a circular cloud of about 3.3 km diameter. All the clouds with size equal to or less than three pixels were discarded by the cloud summary program. The percent cloud-cover over the whole area was obtained as the total of all clouds defined in this manner.

There were several categories employed to separate clouds according to their size as follows:

1. Tiny clouds, less than 4 pixels, corresponding to a circular cloud diameter less than 3.3 km, were neglected here.
2. Isolated convective clouds:
  - (a) Small clouds, 4 to 7 pixels, with an equivalent diameter between 3.3 km and 4.3 km, usually a fair weather cumulus cloud;
  - (b) Medium clouds, with 8 to 37 pixels, having an equivalent diameter between 4.3 km and 10 km, cumulus congestus in most cases;
  - (c) Large clouds, with 38 to 148 pixels and an equivalent diameter between 10 km to 20 km, and usually identified as cumulonimbus;
3. Widespread deep convection or stratiform clouds, with more than 148 pixels, corresponding to an equivalent diameter larger than 20 km, are identified as a widespread deep convective cloud for high mean brightness or as area of stratiform cloud for low mean brightness.

The cloud populations in various size categories derived from the cloud summary program are given in Table 1-1. A number of different patterns were found to occur. Large numbers of clouds appeared on 24 June and early on 8 July, with much smaller numbers of clouds on the other two days. Generally speaking, the number of small and medium isolated convective clouds dominated the total number of clouds. As a result, the numerous small and medium isolated clouds of 24 June and early on 8 July led to large total numbers of clouds at these times. However, the percent cloud cover was always dominated by the widespread convective and stratiform clouds, independent of the total cloud number.

The percent cloud cover was computed as the ratio of the number of data points within the cloud boundary, determined by the critical visible value, to the total number of data points within the study area. Figure 1-3 compares the percent cloud cover results over the study area for the four days. On 22 June, cloud cover exceeded 80% much of the day. Large percent cloud cover also occurred during the late afternoon of 8 July. The early afternoon of both 24 and 27 June was dominated by small isolated clouds, which kept the cloud cover small and even clear for the first four data times on 27 June. But, on both days in the late afternoon, a storm moved into the study area from the west, contributing to increased cloud cover over the study area. Of interest are the contrasting cases of large percent cloud cover contributed by only a few clouds and small percent cloud cover despite the presence of many clouds. The cloud cover at 2045 GMT, 22 June was 87%, although there were only 5 separate clouds at this time. The percent cloud cover at 1845 GMT, 24 June was only 6.1%, despite the presence of 60 clouds in the study area.

The visible brightness frequency distribution curves for four selected times at two-hour intervals are shown in Figures 1-4 through 1-7. In each figure, the abscissa is the difference of individual brightness values relative to the critical value distinguishing cloud from non-cloud background for the given time. The appearance of the brightness distribution curves is closely related to the percent cloud cover at the corresponding time. A comparison between Figure 1-3 and Figures 1-4 through 1-7 shows

Table 1-1 Number of clouds of different sizes

TIME (GMT)	22 June				24 June				27 June				8 July			
	<u>2a</u> *	<u>2b</u> *	<u>2c</u> *	<u>3</u> *	<u>2a</u>	<u>2b</u>	<u>2c</u>	<u>3</u>	<u>2a</u>	<u>2b</u>	<u>2c</u>	<u>3</u>	<u>2a</u>	<u>2b</u>	<u>2c</u>	<u>3</u>
1745	-	-	-	-	20	28	7	3	0	0	0	0	33	36	5	3
1815	4	4	1	1	27	26	7	2	0	0	0	0	-	-	-	-
1845	1	2	3	3	30	24	4	2	1	0	0	0	27	28	6	5
1915	5	7	0	1	28	26	9	3	1	1	0	0	15	17	5	4
1945	6	5	2	2	25	32	3	4	0	2	3	0	14	15	5	4
2015	2	5	0	1	33	35	7	3	6	1	2	2	15	7	0	1
2045	1	3	0	1	29	31	5	5	4	6	2	3	-	-	-	-
2115	6	15	1	1	24	22	7	4	10	12	1	1	12	12	0	1
2145	12	19	4	2	-	-	-	-	-	-	-	-	-	-	-	-
2215	7	12	2	3	20	10	2	1	5	11	5	2	-	-	-	-
2245	6	5	0	1	4	4	1	1	-	-	-	-	7	13	4	1
2315	11	3	2	2	10	10	2	2	-	-	-	-	-	-	-	-
2345	2	3	1	1	13	19	5	2	-	-	-	-	10	19	4	1
0015	8	7	2	1	15	8	2	2	-	-	-	-	5	9	2	1

\*2a: Small convective: diameter between 3.3 km to 4.3 km

\*2b: Medium convective: diameter between 4.3 km to 10 km

\*2c: Large convective: diameter between 10 km to 20 km

\* 3: Widespread: diameter larger than 20 km

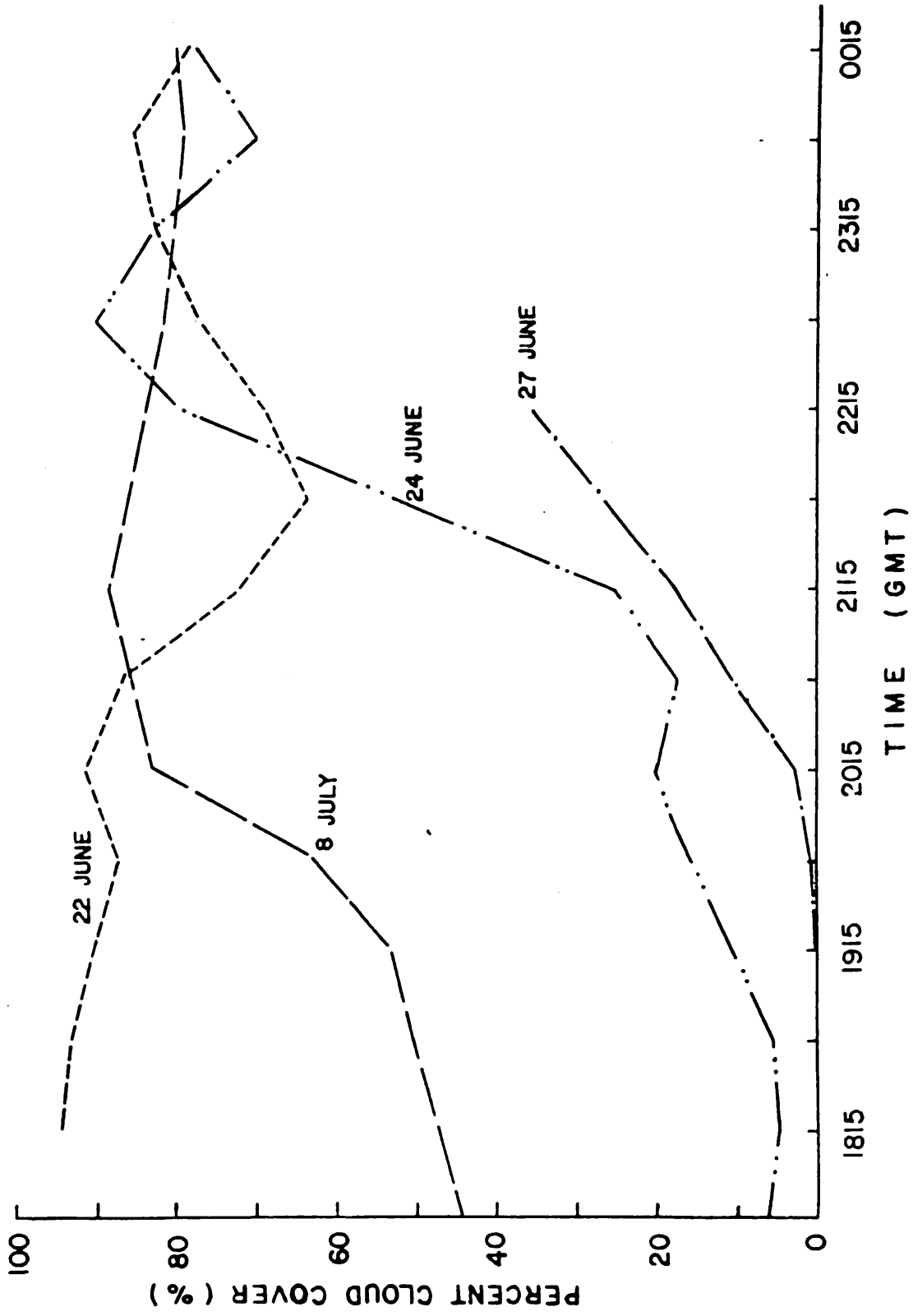


Figure 1-3 Variation of percent cloud cover with time.

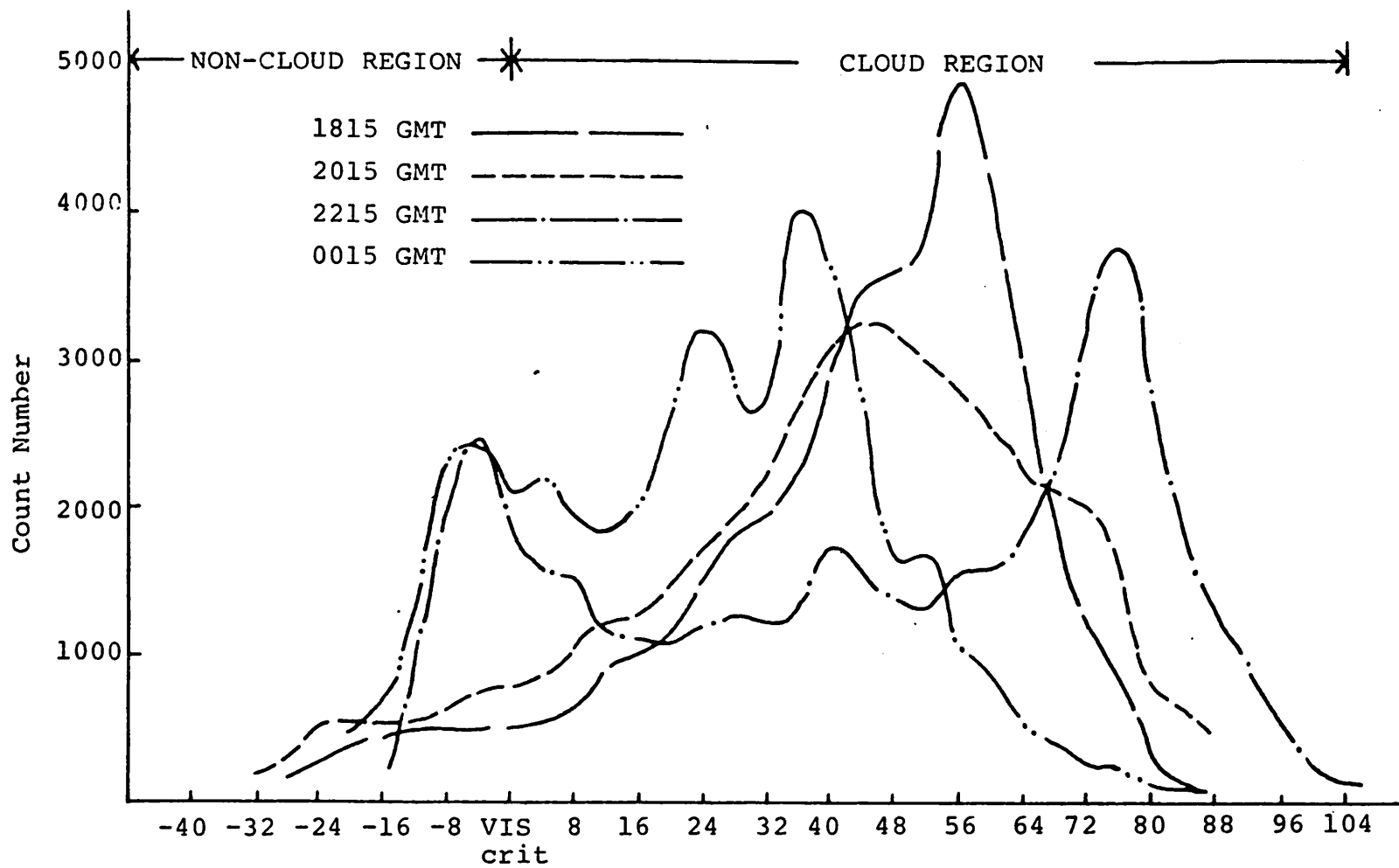


Figure 1-4 Curves of the frequency distribution of visible radiance values on 22 June.

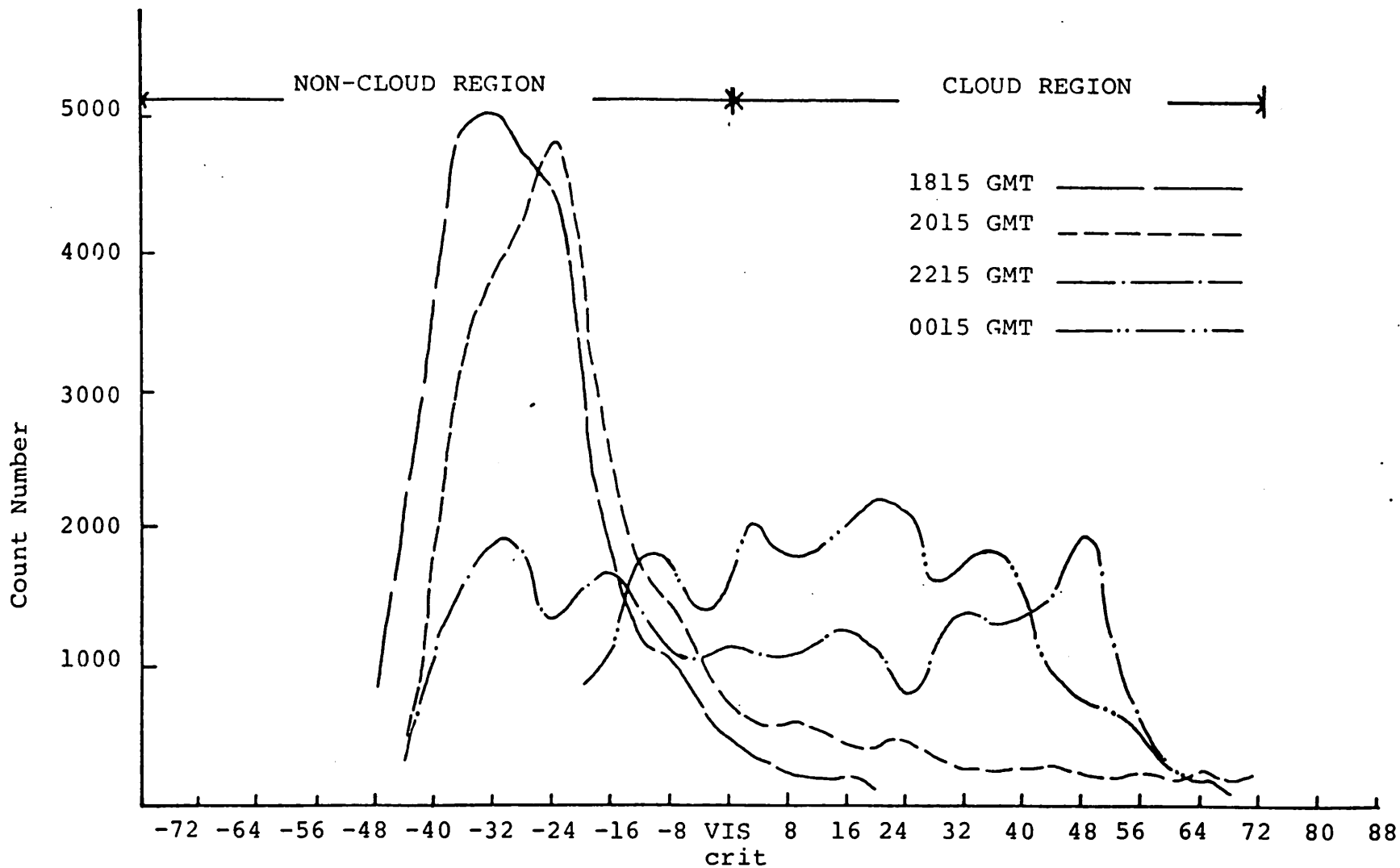


Figure 1-5 Curves of the frequency distribution of visible radiance values on 24 June.

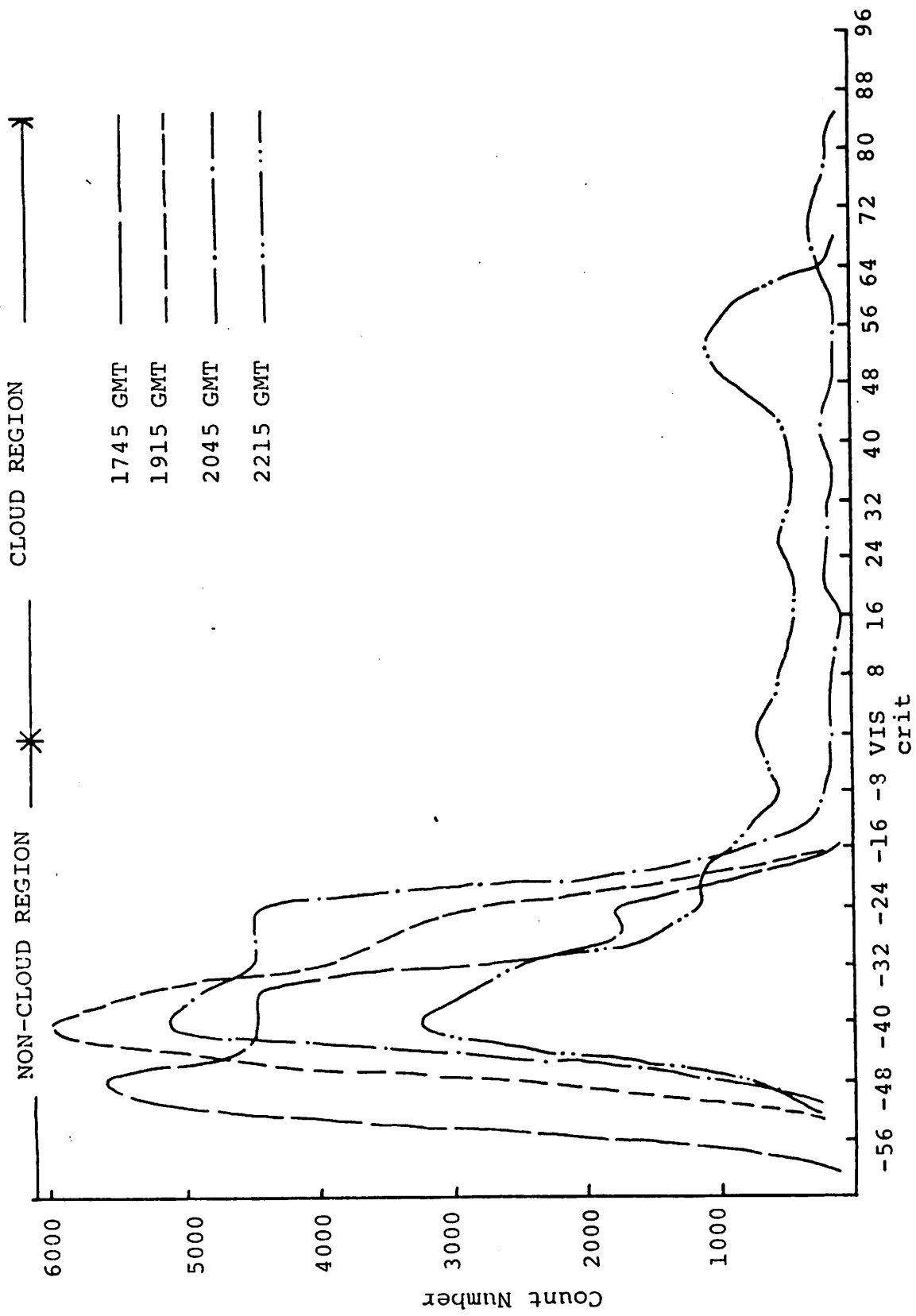


Figure 1-6 Curves of the frequency distribution of visible radiance values on 27 June.

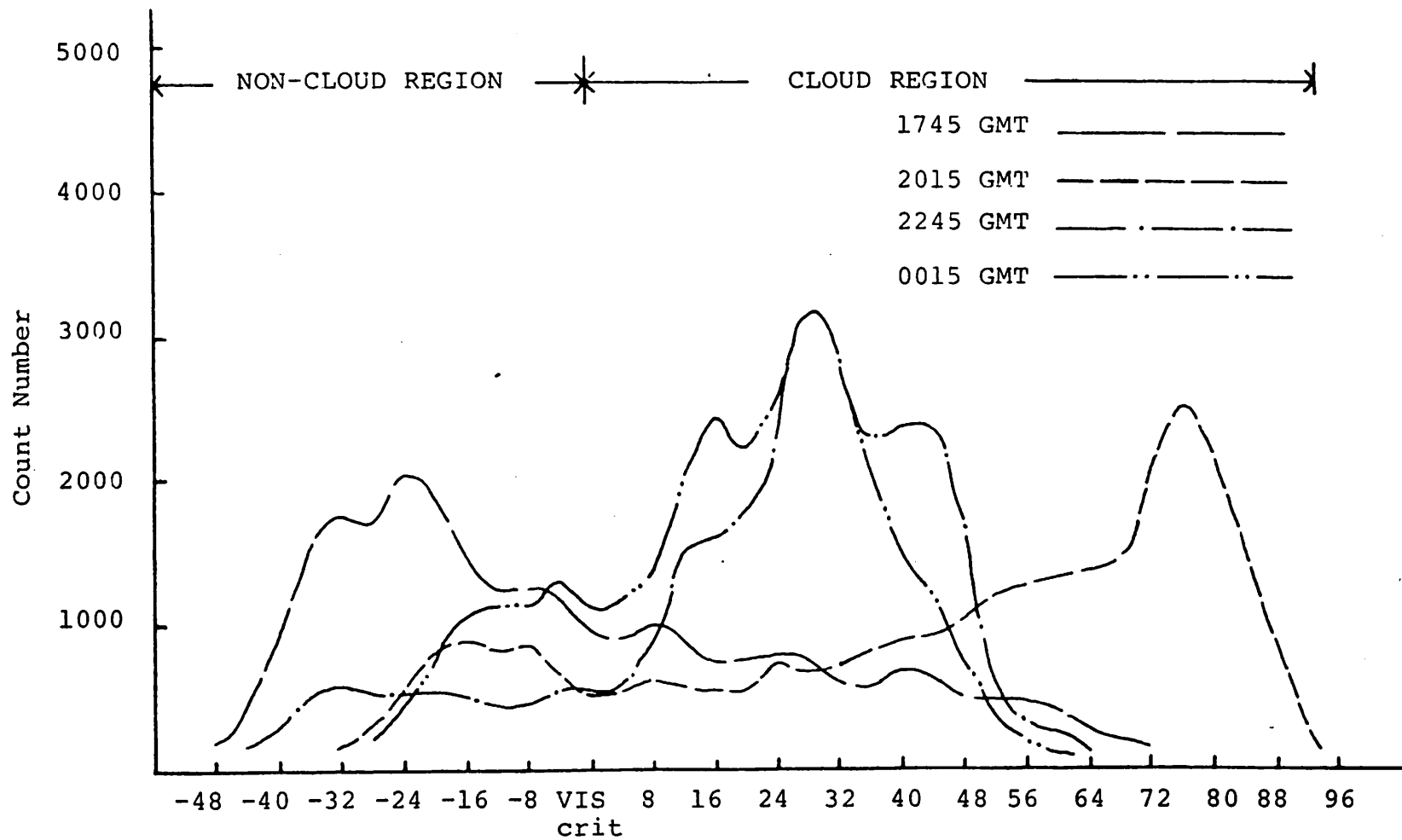


Figure 1-7 Curves of the frequency distribution of visible radiance values on 8 July.

that large cloud cover (greater than 70%) occurred when the mode of the brightness distribution curve was positive, and that small cloud cover (less than 45%) corresponded to a negative modal value.

The modal values at 1815 and 2015 GMT on 22 June and 0015 GMT on 23 June were from 40 to 60 units greater than the critical visible value at those times and the mode at 2215 GMT was 76 units above the critical value. The pattern on 8 July had a similar distribution, except for the curve at 1745 GMT, early in the day. The mode at 2015 GMT was 76 units greater than the critical value, as was also observed at 2215 GMT on 22 June. At all of these times the total cloud cover was at least 80%. The most substantial rainfalls observed on the case study days occurred at these times. For both 22 June and 8 July the visible radiance values in the cloud region of the frequency distribution curve were skewed toward large positive values.

The patterns for 24 and 27 June are similar, but very different from those on 22 June and 8 July. On these two days, the brightness frequency distributions were concentrated in the non-cloud region. The modes at 1815 and 2015 GMT on 24 June were located 32 and 24 units, respectively, below the corresponding critical values. Late that afternoon, a cloud system moved into the study area and the pattern of distribution curves at 2215 and 0015 GMT was significantly changed. The patterns on 27 June were all uniformly concentrated in the non-cloud region, with modal values at the four selected times all from 40 to 48 units below the critical visible value for each time. At all of these times, the cloud cover was less than 35%. In contrast to the 22 June and 8 July curves, the visible radiance values in the cloud region on 24 and 27 June were quite uniformly distributed over all positive values. The precipitation analyses from the raingage network for these four days support the tentative conclusion that the visible data brightness value distribution curves are correlated with rainfall.

Comparisons of percent cloud cover and cloud numbers derived from satellite radiance data and from photographic imagery are shown in Table 7-2 at one-hour intervals. Although agreement between the two sets of results is generally good, there are some instances of poor agreement. In the original analysis of the photographic imagery, the study area was divided

Table 1-2 Comparison of percent cloud cover and cloud numbers from satellite radiance data and photographic imagery.

<u>DAY</u>	<u>Time (GMT)</u>	<u>Percent Cloud Cover</u>		<u>Number of Widespread Clouds</u>		<u>Number of Isolated Clouds</u>		<u>Total Number of Clouds</u>	
		<u>Radiance</u>	<u>Imagery</u>	<u>Radiance</u>	<u>Imagery</u>	<u>Radiance</u>	<u>Imagery</u>	<u>Radiance</u>	<u>Imagery</u>
22 June	1930	93.5	88	2	1	6.5	42	8.5	43
	1930	89.1	84	1.5	2	12.5	92	14	94
	2030	89.2	81	1	2	5.5	100	6.5	102
	2130	68.3	59	1.5	1	28.5	105	30	106
	2230	73.6	54	2	1	16	37	18	38
	2330	-	-	-	-	-	-	-	-
23 June	0030	79.3	65	1	1	17	12	18	13
24 June	1730	6.4	32	3	3	55	247	58	250
	1830	5.4	9	2	1	59	218	61	219
	1930	13.6	23	3.5	2	61.5	284	65	286
	2030	18.7	9	4	2	70	96	74	98
	2130	25.4	20	4	3	73	70	77	73
	2230	84.8	28	1	2	20.5	27	21.5	29
	2330	76.9	49	2	3	29.5	0	31.5	3
25 June	0030	78.4	51	2	1	25	5	27	6

Table 1-2 Continued

<u>DAY</u>	<u>Time (GMT)</u>	<u>Percent Cloud Cover</u>		<u>Number of Widespread Clouds</u>		<u>Number of Isolated Clouds</u>		<u>Total Number of Clouds</u>	
		<u>Radiance</u>	<u>Imagery</u>	<u>Radiance</u>	<u>Imagery</u>	<u>Radiance</u>	<u>Imagery</u>	<u>Radiance</u>	<u>Imagery</u>
27 June	1730	0	0	0	0	0	0	0	0
	1830	0	0	0	0	0	0	0	0
	1930	0.3	5	1.5	0	2	7	3.5	7
	2030	6.6	5	2.5	1	0.5	30	13	31
	2130	17.8	11	1	1	23	66	24	67
	2230	35.2	32	2	2	21	34	23	36
8 July	1730	43.6	57	3	3	74	323	77	326
	1830	50.1	53	5	3	61	256	66	259
	1930	58.4	61	4	2	35.5	247	39.5	249
	2030	82.8	73	1	1	22	191	23	192
	2130	90.9	79	1	1	24	176	25	177
	2230	81.9	83	1	1	24	78	25	79
	2330	79.2	70	1	1	33	80	34	81
9 July	0030	80.2	73	1	2	16	73	17	75

into nine sub-areas, as shown in Figure 1-2. In the comparison presented here, these individual values of percent cloud cover were averaged to produce a more representative overall estimate. Further, the number of isolated and widespread clouds for the whole study area was obtained by adding the numbers from each sub-area. Table 1-2 compares the percent cloud cover and cloud number results derived from these two sources.

The agreement of percent cloud cover between the two sets is good, except for a few cases on 24 June. Because the percent cloud cover from photographic imagery was estimated visually, it was difficult to maintain as consistent an accuracy as with percent cloud cover derived from radiance data. In general, the difference in percent cloud cover estimated from these two data sets was approximately 5% to 10%. The most difficult estimates of percent cloud cover occurred at times when isolated, cluster or line clouds were predominant. This situation was particularly true on 24 June, where the differences in Table 1-2 are very noticeable.

The agreement in Table 1-2 in number of widespread clouds between these two data sets is seen to be much better than that for isolated clouds. Especially on 24 June, when isolated clouds dominated, the agreement was very poor. A detailed study of the results on this date points to an explanation. The computer cloud summary program treated many small clouds as a single large cloud as long as the individual clouds were linked together at even one point. As a result, the number of widespread clouds was one or two more than the value derived from the imagery, while the number of isolated clouds was much less than that from imagery. Early on 8 July, the number of isolated clouds differed for the same reason, although the numbers of the widespread clouds were nearly equal.

Another factor influencing the accuracy of these results was the variation in solar zenith angle, which increased to  $50^{\circ}$  after 2230 GMT; consequently, the brightness of the scene was significantly reduced. Under these conditions, fewer small isolated clouds could be distinguished from the underlying surface in the photographic imagery. The late afternoons of 24 June and 8 July are good examples of this problem.

In conclusion, the results derived from radiance data analyzed by the summary program are considered to be more accurate and quantitative. However, analysis of the imagery can be of assistance to the study of radiance data sets, especially in providing a large-scale view of the overall synoptic pattern existing at a given time.

## Task 2. Integration of Satellite Data with Raingage and Radar Measurements

The satellite-derived cloud properties derived in Task 1 have been compared with raingage and radar data in an effort to establish the reliability of the satellite results. All four case study days were treated; however, the presentation here will be limited to a single day, 8 July. A complete discussion of the four case study days will be given in a technical report to be submitted in the near future. Utilizing the available satellite, radar and precipitation data, a comparison was made by placing the three different data sources into a common coordinate system. The reference coordinates have been selected to be the rectangular array of visible satellite radiance measurements used in this study. The objective of this comparison was to enhance understanding of (a) the structure of the convective clouds (b) the relation between organized mesoscale features and the synoptic scale (c) storm development processes, and (d) precipitation mechanisms.

Two weak cold fronts extended from the northeastern United States through the central United States into Texas at 1500 GMT on 8 July 1977. The cold fronts moved slowly eastward and passed through the study area at 1800 GMT, just before heavy rainfall was detected in the raingage network (Figure 2-1). During the next three-hour interval, the fronts moved eastward and left the study area by 0000 GMT 9 July, as the rainfall subsided.

A distinct ridge and trough pattern was present at 500 mb on 8 July. The ridge passed through the New Mexico area at 1200 GMT and remained stationary until 0000 GMT 9 July. Cold air advection occurred within the study area at the 500 mb level.

The recording raingage network in 1977 consisted of 59 stations and recorded rainfall to the nearest one-hundredth inch for every 15-minute

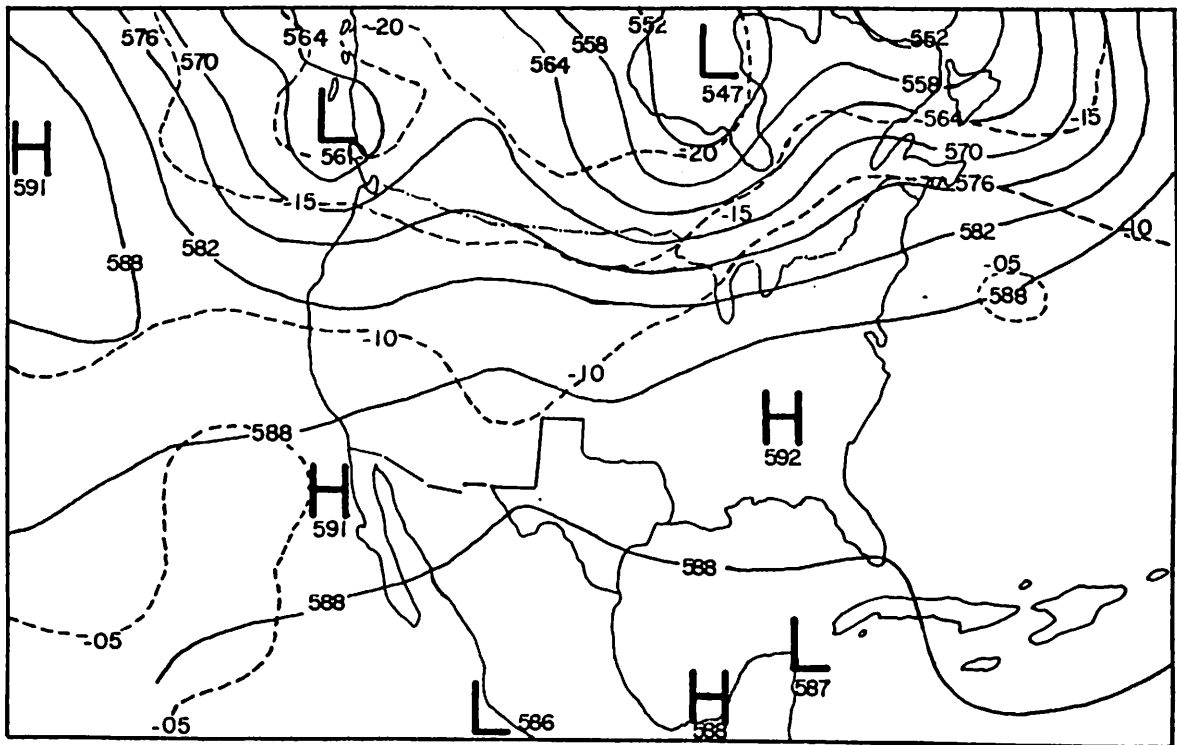
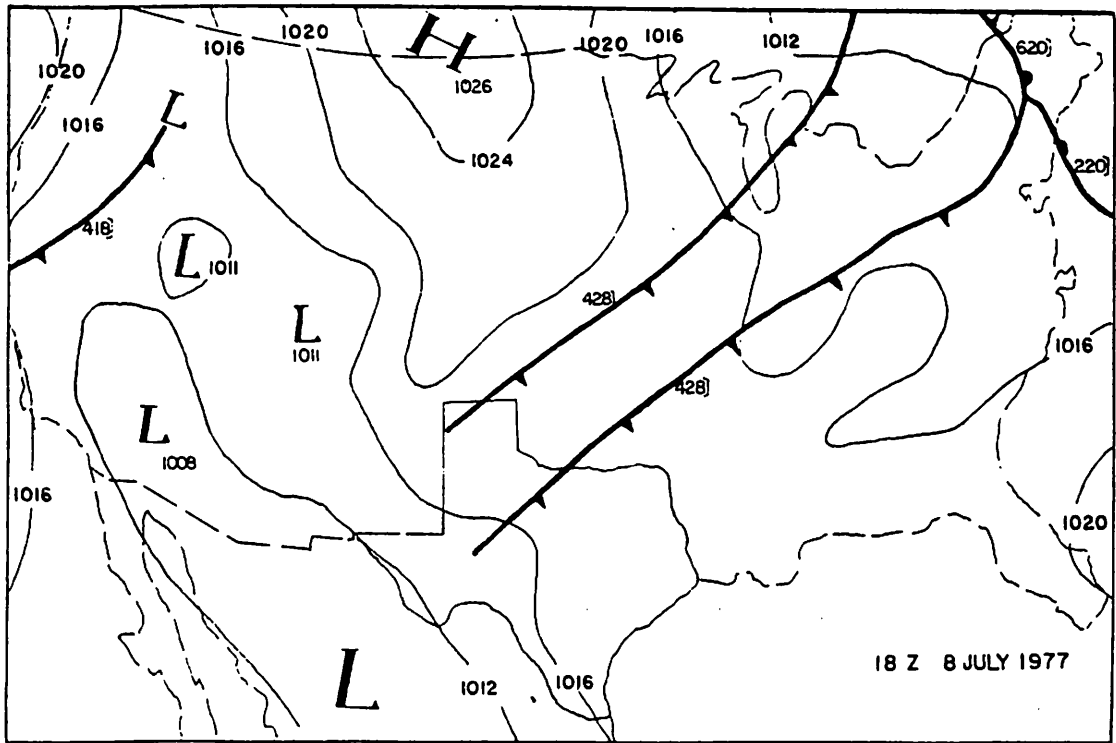


Figure 2-1 Surface chart at 1800 GMT and 500 mb chart at 1200 GMT on 8 July 1977.

interval. The precipitation analysis indicated that the precipitation on 8 July was concentrated in the afternoon, from 1830 to 2045 GMT, when a line of intense rainfall formed in association with the passage of the two cold fronts through the raingage network. The rain subsided within the raingage network soon after the cold fronts moved out of the study area. The variation with time of total precipitation volume on 8 July is shown in Figure 2-2. The value plotted at a given time represents the rainfall occurring during the preceding 15-minute interval. The spatial pattern of total rainfall from 1800 to 0000 GMT 9 July (Figure 2-3) shows that the heavy rainfall areas were located in a band stretching from southwest to northeast, with many stations collecting over 1.5 inches during this six-hour interval. The broken isohyet in Figure 2-3 represents a rainfall of 0.01 inch and the solid contours are given for every 0.25 inch. The total surface water produced by precipitation was found to be 66,095 acre-ft, the heaviest rain among the four case study days.

The highly modified M-33 radar located at Winston Field in Snyder, Texas, provided the digital data for this case study day. Figure 2-4 shows PPI plots from the M-33 radar on 8 July 1977. The borders of the raingage network and satellite study area are drawn over the radar echo pattern. The plot for 1948 GMT shows that a cluster of strong reflectivity cells located in the central portion of the raingage network passed through the Snyder area, although no data were available within 25 km of the radar site because of the range delay. The rainfall pattern during the period 1930-1945 GMT verified that a heavy rain band passed through this area, producing more than 0.80 inch within 15 minutes at two stations. The rain band structure persisted until 2018 GMT, maintaining the same appearance in the precipitation pattern. The rainfall intensity decreased rapidly after 2015 GMT, although the rainfall area remained in the central portion of the raingage network. The PPI plots show that the echo area became more widespread later, but that reflectivity values weakened. The precipitation analysis and digital PPI plots were in good agreement on this point. The satellite visible data showed increases in the percent cloud cover and in the area covered by the brightest clouds early in the study period, reaching maximum values near 2015 GMT, as was observed in the precipitation pattern.

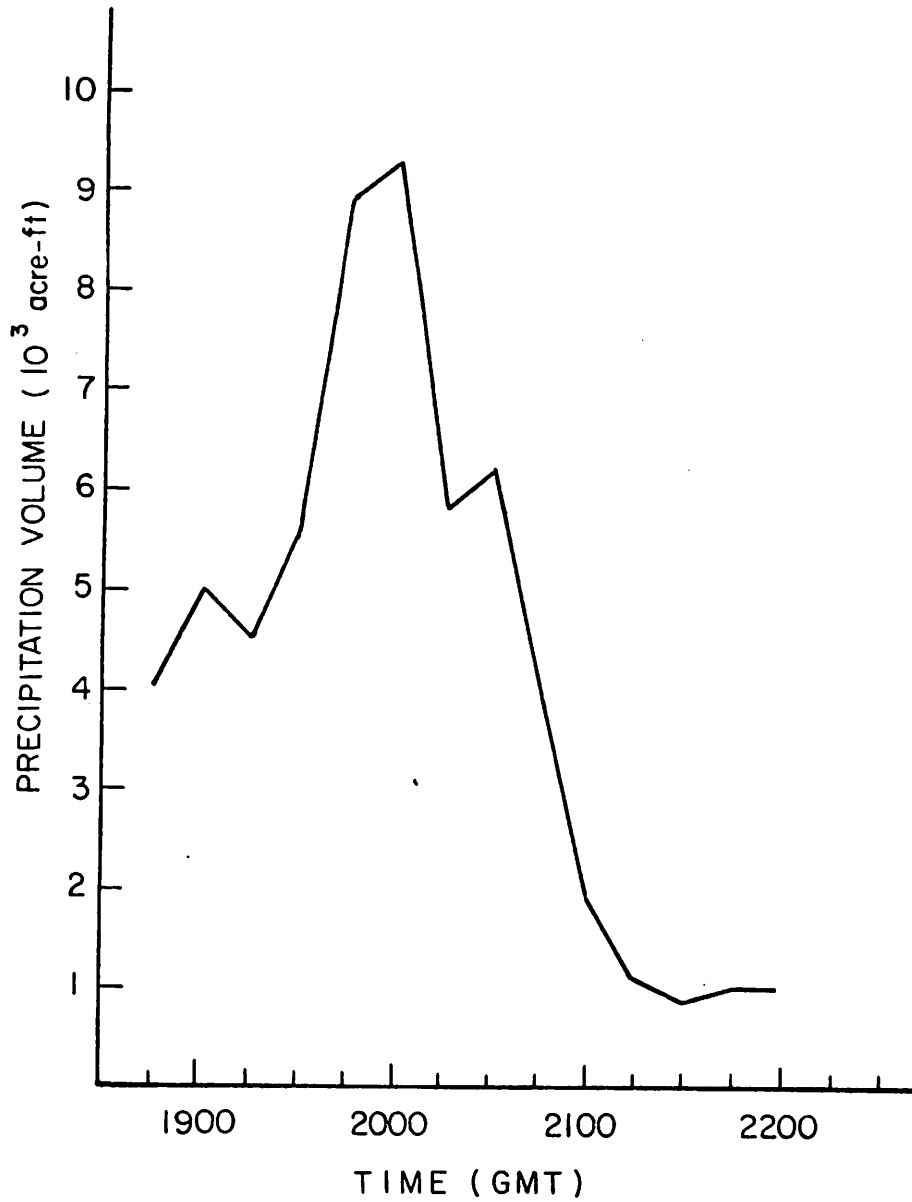


Figure 2-2 Variation of total network precipitation with time on 8 July 1977.

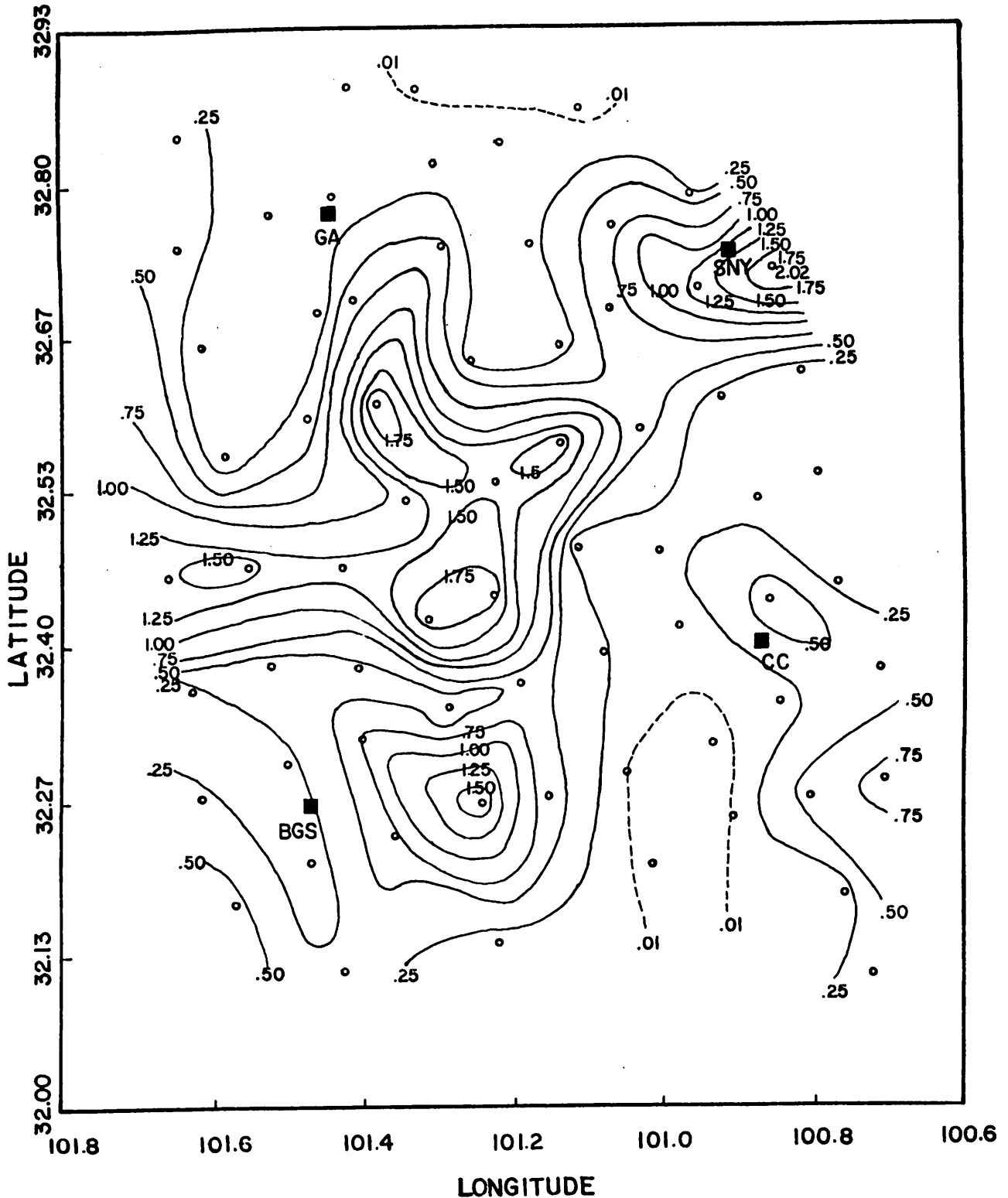


Figure 2-3 Precipitation analysis of the total precipitation from 1800 GMT 8 July to 0000 GMT 9 July 1977. The isohyets are labelled in inches.

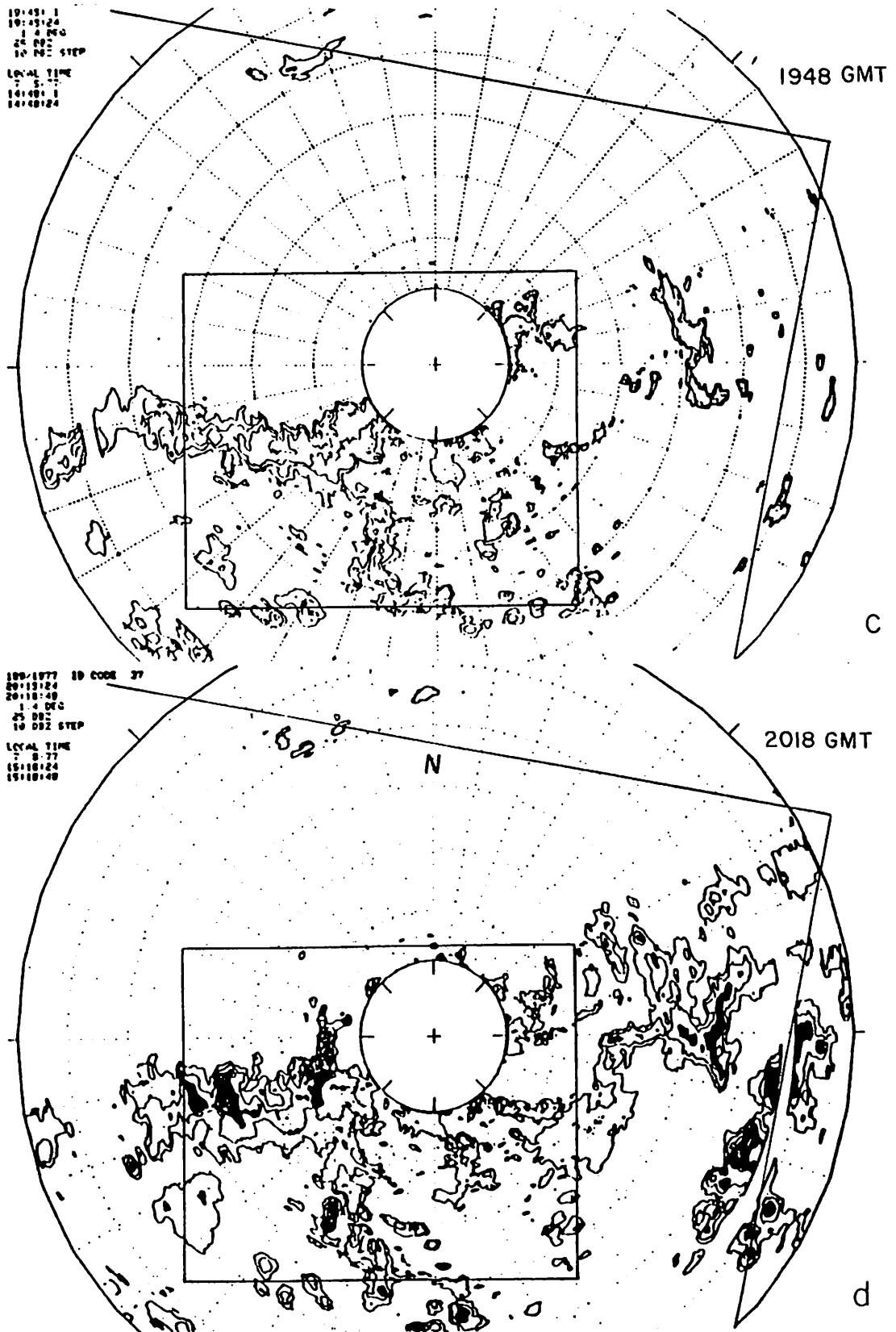


Figure 2-4 PPI displays on 8 July 1977 from the M-33 radar at Snyder. The outer boundary shows the study area, while the inner box is for the rain gauge network. The echo threshold is 25 dBz and dark solid areas represent reflectivities greater than 45 dBz.

The latitude and longitude coordinates of each raingage station have been located in the satellite radiance data arrays. After plotting the raingage data, isohyetal patterns were constructed in the transformed coordinate system for comparison with the radiance data. Note that the reference coordinate system was selected to be the rectangular array of visible satellite radiance data.

The rain began in the interval 1830-1845 GMT, as was shown in Figure 2-2. The sequence of diagrams in Figure 2-5 shows the relative location of cloud albedo, cloud top temperature and the rain area. Note that only the coldest isotherms are shown in any given frame in Figure 2-5. The diagram at 1845 GMT shows that the most intense rain area was located under the brightest and coldest cloud tops within which the cloud albedo was larger than 0.63 and the corresponding cloud top height was above 13 km. More than 0.5 inch of rain had occurred within the previous 15 minutes. A strong rain band along a line from Snyder to Big Spring formed soon after the rain began, and is the rain band detected in the PPI radar plots of Figure 2-4. The maximum precipitation occurring within the rain band was located under clouds with either high albedo or high tops, or both. The rainfall intensity increased sharply after 1915 GMT when the clouds over the raingage network developed tops to approximately 14.5 km and the area of albedo greater than 0.63 increased considerably. The precipitation peak was reached just before 2000 GMT. Meanwhile, at 2015 GMT the raingage network was totally covered by bright and high-topped clouds with albedos over 0.63 and top heights above 15 km. The PPI digital radar analysis also indicated that the reflectivity gradients within the rain band became quite sharp, attaining values greater than 55 dBz at this time. The rainfall intensity decreased rapidly after the precipitation peak and little precipitation was recorded after 2130 GMT.

Three RHI plots for 1942 GMT were taken along the azimuth angles  $200^{\circ}$ ,  $235^{\circ}$ , and  $242^{\circ}$  with respect to Snyder. Figure 2-6 shows the isohyet pattern for the period 1945-2000 GMT, upon which lines are drawn marking the three cross sections investigated. The cross section along the line BB' in Figure 2-6 contained intense reflectivity values, as evidenced by a raingage measurement at 32 km range of 0.80 inch within 15 minutes (Figure 2-7). Cross

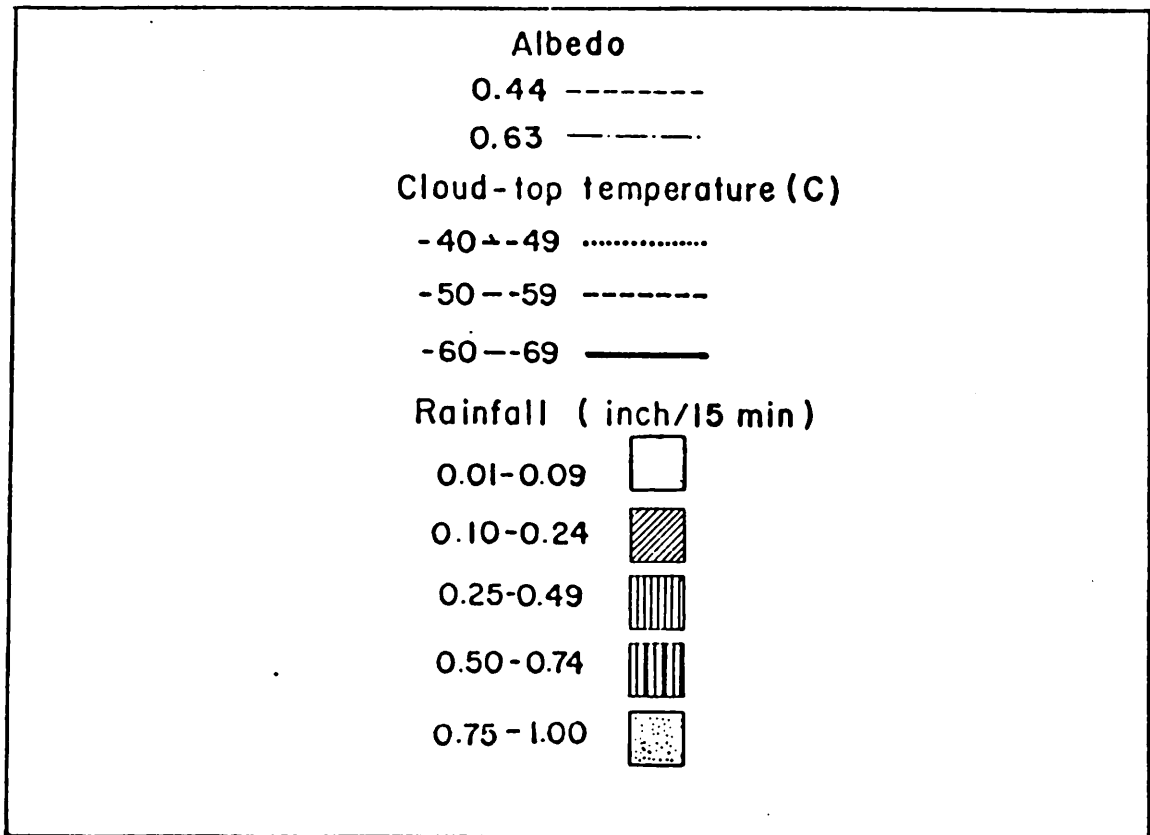
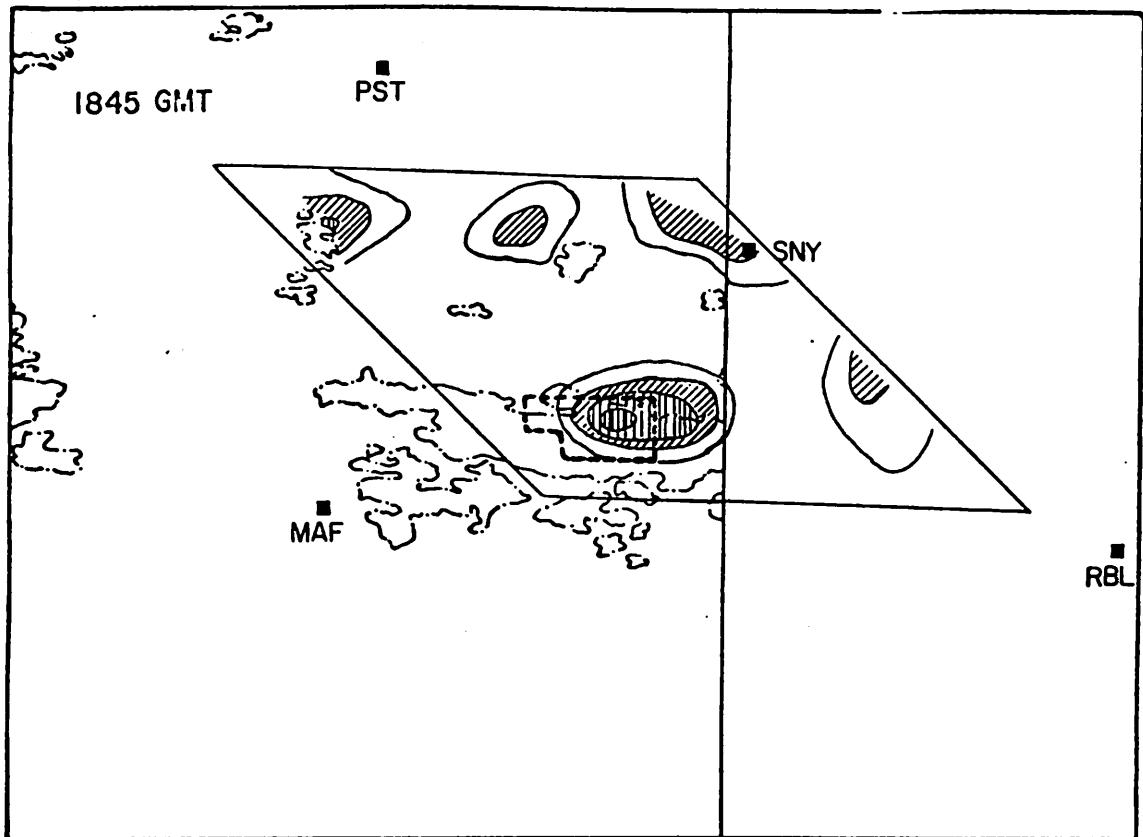


Figure 2-5 Cloud albedo, cloud top temperature and rainfall intensity on 8 July 1977.

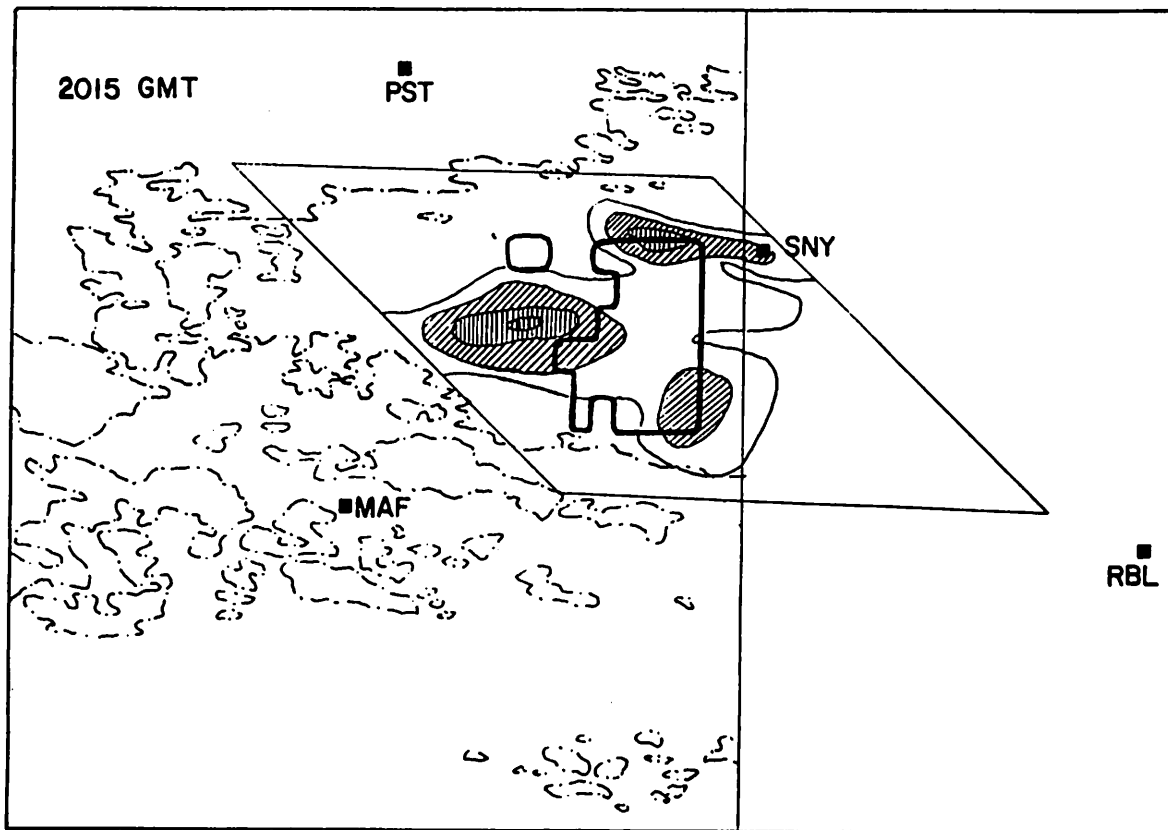
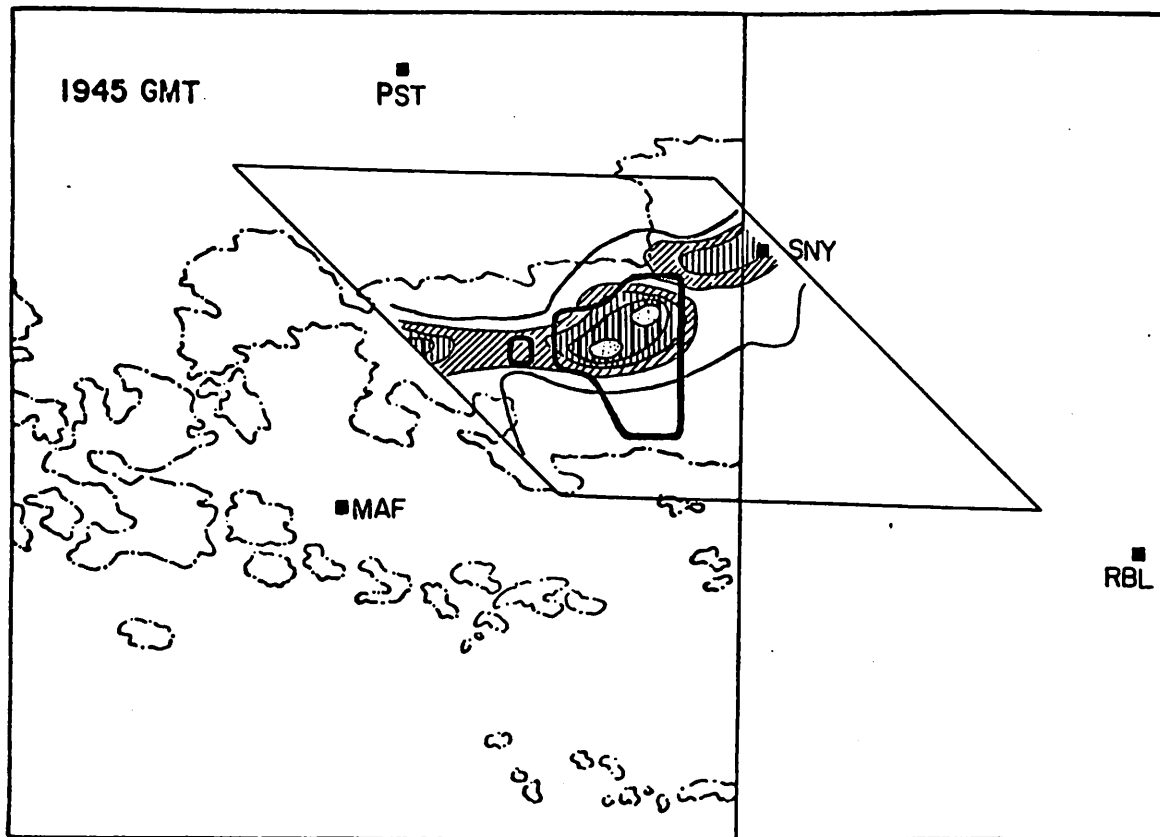


Figure 2-5 Continued

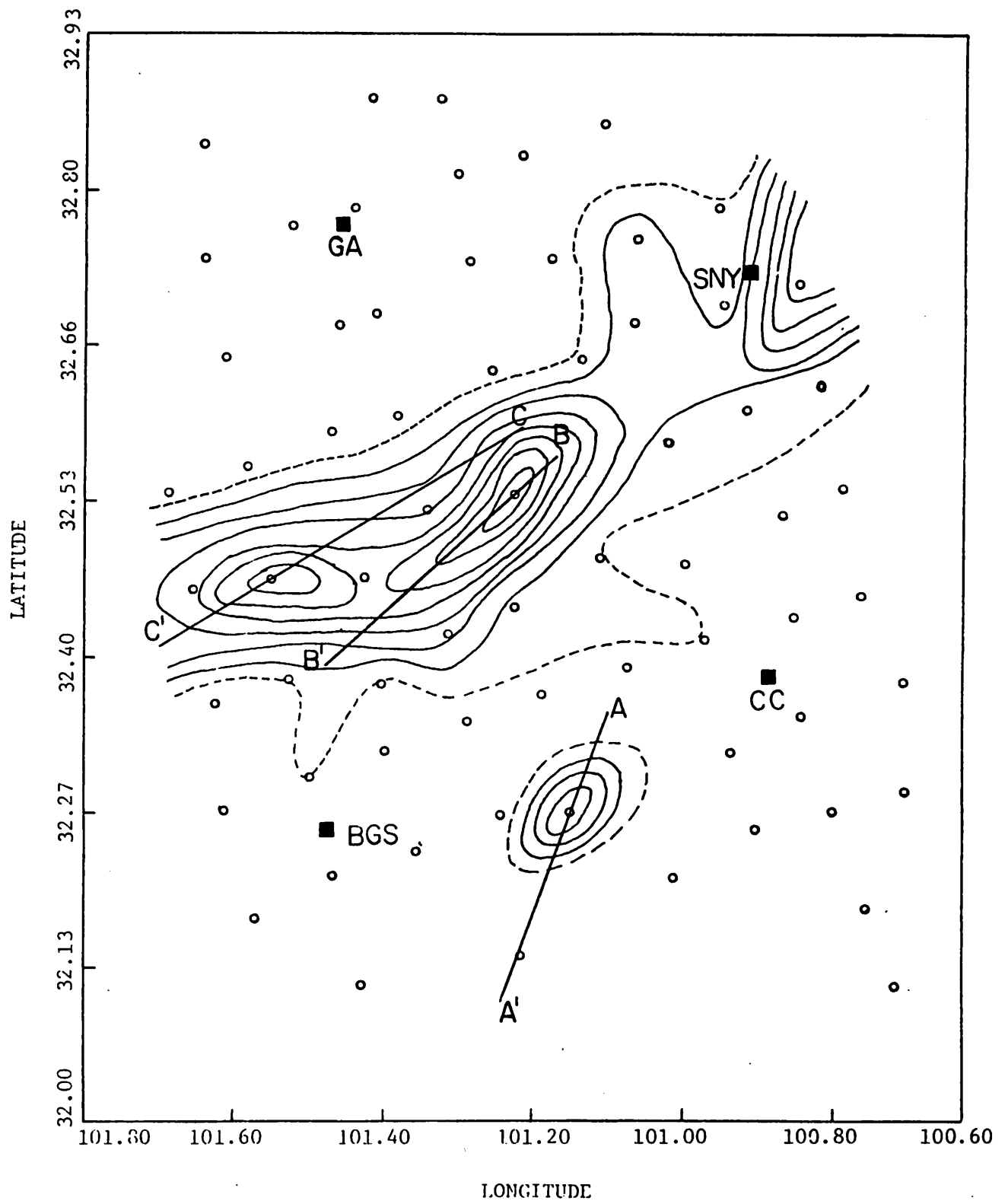


Figure 2-6 Isohyet pattern for the period 1945-2000 GMT 8 July 1977. The dashed line is the isohyet for 0.01 inch, and the solid lines are contoured with a threshold of 0.1 inch and given in 0.1 inch increments.

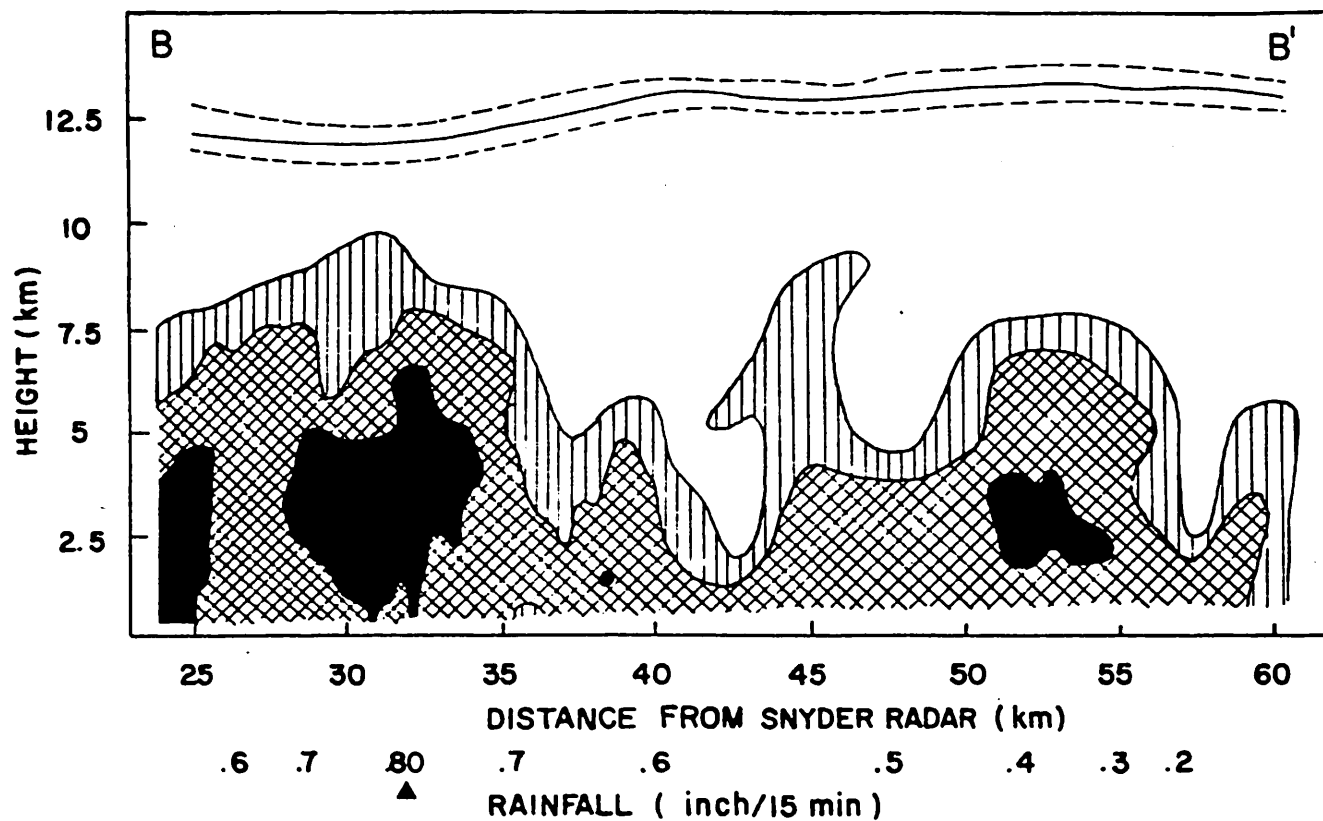


Figure 2-7 RHI display derived from M-33 radar for the azimuth angle  $235^{\circ}$  at 1942 GMT 8 July 1977. The threshold is 30 dBz and is contoured in 10 dBz increments. The upper solid line is the cloud top height derived from satellite infrared data and the dashed lines correspond to a temperature uncertainty of  $\pm 3$  C. Also shown are rainfall analysis results with actual rainage measurements marked by  $\Delta$ .

section BB' has been located directly within the rain band structure identified in the PPI plots of Figure 2-4. If the commonly used Z-R relationship  $Z = 200 R^{1.6}$  is employed to infer an approximate rainfall intensity, one obtains a rainfall under the intense reflectivity center of 0.9 inch over a 15-minute interval. This is rather good agreement, considering that a different Z-R relation might be appropriate or that evaporation below the cloud base may have occurred. The satellite-derived cloud tops remained uniform in height along the length of the cross section. In addition to the actual estimated heights, the cloud top estimates which would result from cloud top temperature errors of 3 C have been shown in order to provide a measure of the uncertainty (seen to be approximately 1 km) in cloud top height associated with what is often considered to be a reasonable estimate of the error in cloud top temperature measurements. The minimum detectable signal at 1942 GMT on 8 July was 30 dBz. Therefore, the top of the precipitation-particle produced echo detected by radar at 1942 GMT was considerably below the cloud top detected with the satellite infrared data.

Four RHI cross sections at 2018 GMT along azimuth angles  $211^{\circ}$ ,  $223^{\circ}$ ,  $253^{\circ}$  and  $259^{\circ}$  were studied because each of them passed through an intense storm (Figure 2-8). The minimum detectable signal at this time was about 17 dBZ, resulting in considerably higher radar echo tops, reaching 13 km, than were seen at 1942 GMT. The satellite-derived cloud top heights were closer to the radar reflectivity heights at this time because of the smaller detectable signal.

The cross section at an azimuth angle of  $253^{\circ}$  is shown by line FF' in Figure 2-8. This line passed through the most intense rainfall area at this time which was located inside the rain band discussed earlier (Figure 2-9). The total precipitation measured in the center of this cell over 15 minutes was 0.89 inch, while the reflectivity there was close to 60 dBZ. The gradient of precipitation intensity under the strong storm cell was sharp with the heaviest rain occurring immediately under the intense reflectivity core. The radar reflectivity under that strong storm cell was about 55 dBZ, inferring 0.98 inch of rain within 15 minutes from the assumed Z-R relation. The satellite-derived cloud heights were quite uniform over the intense reflectivity area, but decreased rapidly beyond the storm. The satellite cloud heights and radar echo tops overlapped within the intense radar reflectivity cells. However, the overlap was within the uncertainty

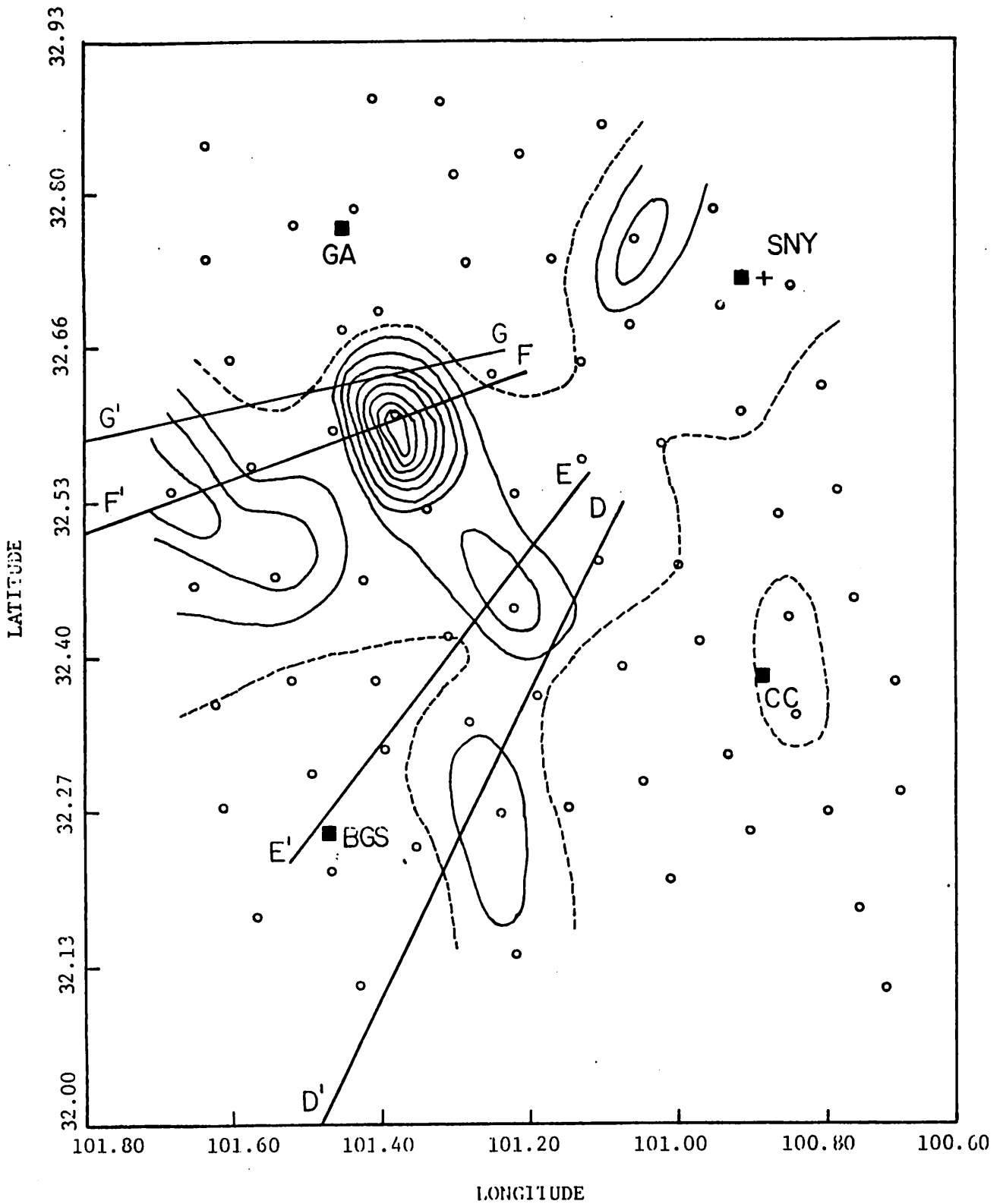


Figure 2-8 Isohyet pattern for the period 2015-2030 GMT  
8 July 1977. Codes are the same as  
Figure 2-6.

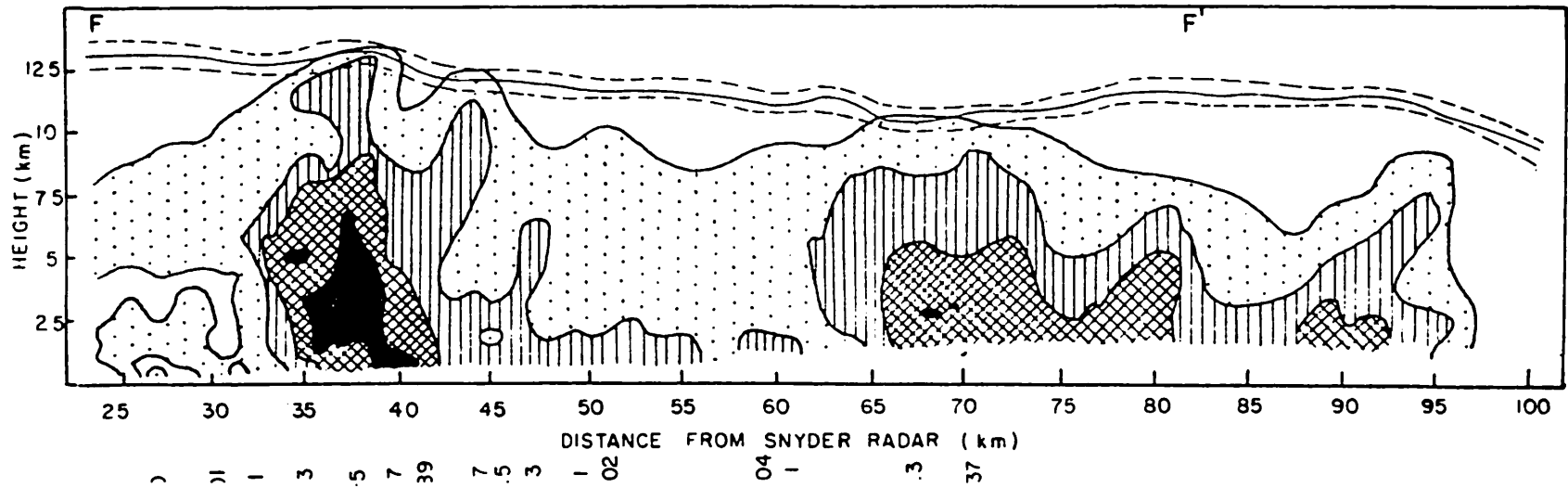


Figure 2-9 RHI display derived from M-33 radar data for the azimuth angle  $253^{\circ}$  at 2018 GMT 8 July 1977. The data threshold is 20 dBz and is contoured in 10 dBz increments. The other codes are the same as in Figure 2-7.

of the satellite-derived cloud top heights. The apparent error in cloud top height can be explained by the fact that each infrared pixel covered a rather large area, about 5.8 x 11.7 km. As a result, the satellite infrared data simply averaged away the presence of smaller cells detectable by radar. Improvement in the spatial resolution of satellite infrared sensors is clearly needed, as this case demonstrates. Nonetheless, the agreement among the several data sets is quite acceptable.

One case of special interest is the cross section along the line GG', for an azimuth angle of 259°. This case is discussed here because the most intense reflectivity at this time occurred along this line (Figure 2-10). The structure was similar to the previous case along FF'. A strong storm cell with large reflectivity gradients was located 35 km from the radar site. This cross section was along the edge of the rain band discussed before, and shown in Figure 2-4. The cloud top heights from the infrared radiances varied from 11 to 12.5 km over two intense storm cells, but decreased rapidly beyond the third storm cell which was located about 80 km from the radar. The agreement between the satellite cloud top heights and radar reflectivity was good along this cross section. A strong reflectivity maximum of more than 60 dBZ was located 35 km from the radar site. It is probable that heavy rain did occur under this intense echo which occurred within the raingage network, but there was no raingage located exactly along this direction. This example illustrates the restrictions associated with interpreting rainfall measurements even from a raingage network with rather dense spacing, and points to the desirability of higher resolution data sources such as radar or satellite measurements.

Atmospheric soundings were made as part of the mesoscale program of Texas HIPLEX. The measurements were made and the data processed by personnel at Texas A&M University. Temperature, moisture and wind were extracted from the soundings at 25 mb intervals. Although the data were available at Midland, Post, Robert Lee and Big Spring, only the soundings at Big Spring are discussed in this study, because it has been determined that, although station-station variations did exist, the temporal changes at a given station were more revealing.

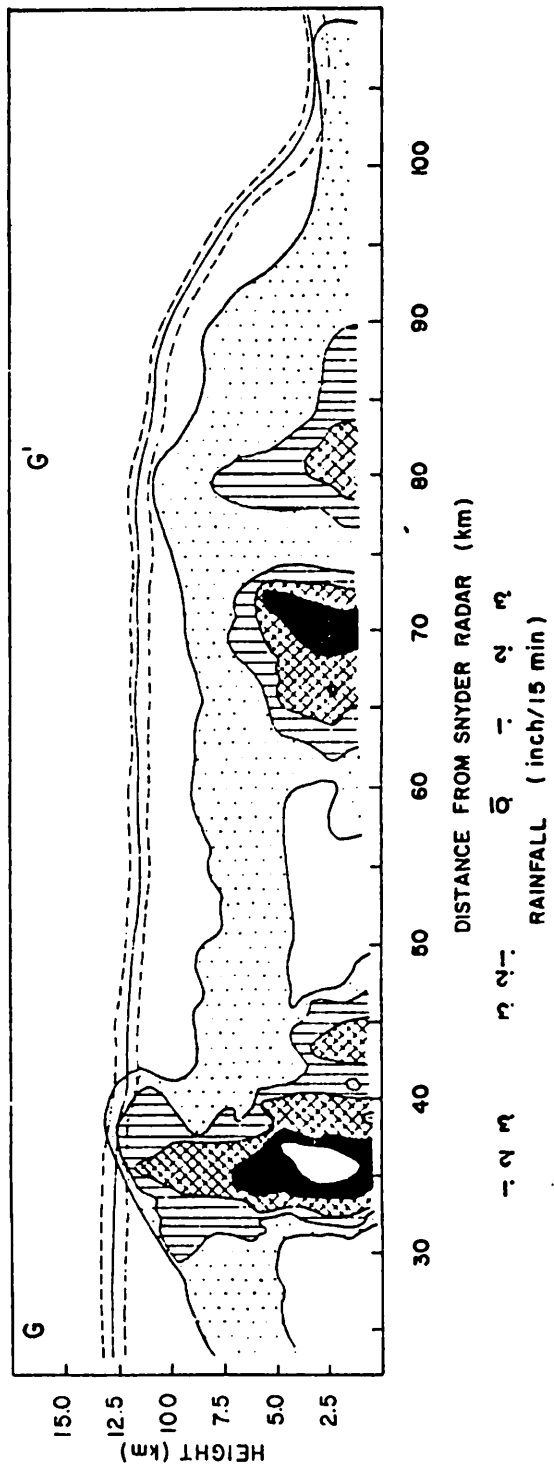


Figure 2-10 Same as Figure 2-9 for azimuth angle 259°.

Figure 2-11 shows the soundings at Big Spring on 8 July. The atmosphere was rather dry at 1500 GMT, but the moisture content then increased rapidly until 1800 GMT. The negative area had disappeared by 18 GMT as the surface warmed up, and convective processes had become likely. Later in the afternoon, the surface was saturated at both 2100 GMT and 0000 GMT 9 July. By this time major precipitation events had occurred. The diamond-shaped appearance of the soundings in the lower layers at both of these times is clearly evident in Figure 2-11. Usually, unsaturated air and subsidence exist in such a region beneath an anvil cloud. The previous discussions have already pointed out that the thunderstorms began to dissipate after 2100 GMT on this day, an observation which is consistent with the above-stated condition.

The most important trigger in this case was the passage of the fronts through the rain gauge network and the study area. All the synoptic, subsynoptic and small-scale features were associated with the movement of these fronts.

A precipitation volume of 66,095 acre-ft, heaviest among four case-study days, was collected from rainfall during the hours the front passed through the study area. A rain band structure was clearly detectable in the precipitation and was oriented parallel to the front. This rain band structure was detected both in the M-33 PPI displays at Snyder and in the satellite imagery. The rain areas, especially the heavy rain area, were located under the brightest clouds (with albedos greater than 0.63) having the highest cloud tops (with cloud tops cooler than  $-50$  C, corresponding to a 12 km height).

Two individual times when the rain band passed through the study area on this day were selected to study RHI cross sections of the M-33 data. In each case, a comparison was made between cloud tops inferred from the radar echoes and from satellite infrared data. Rainfall estimates from a Z-R relationship were also compared to those recorded by the rain gauges. The agreement of these two comparisons was found to be quite good.

Small-scale features on this day provided worthwhile information on thunderstorm development and dissipation associated with movement of the

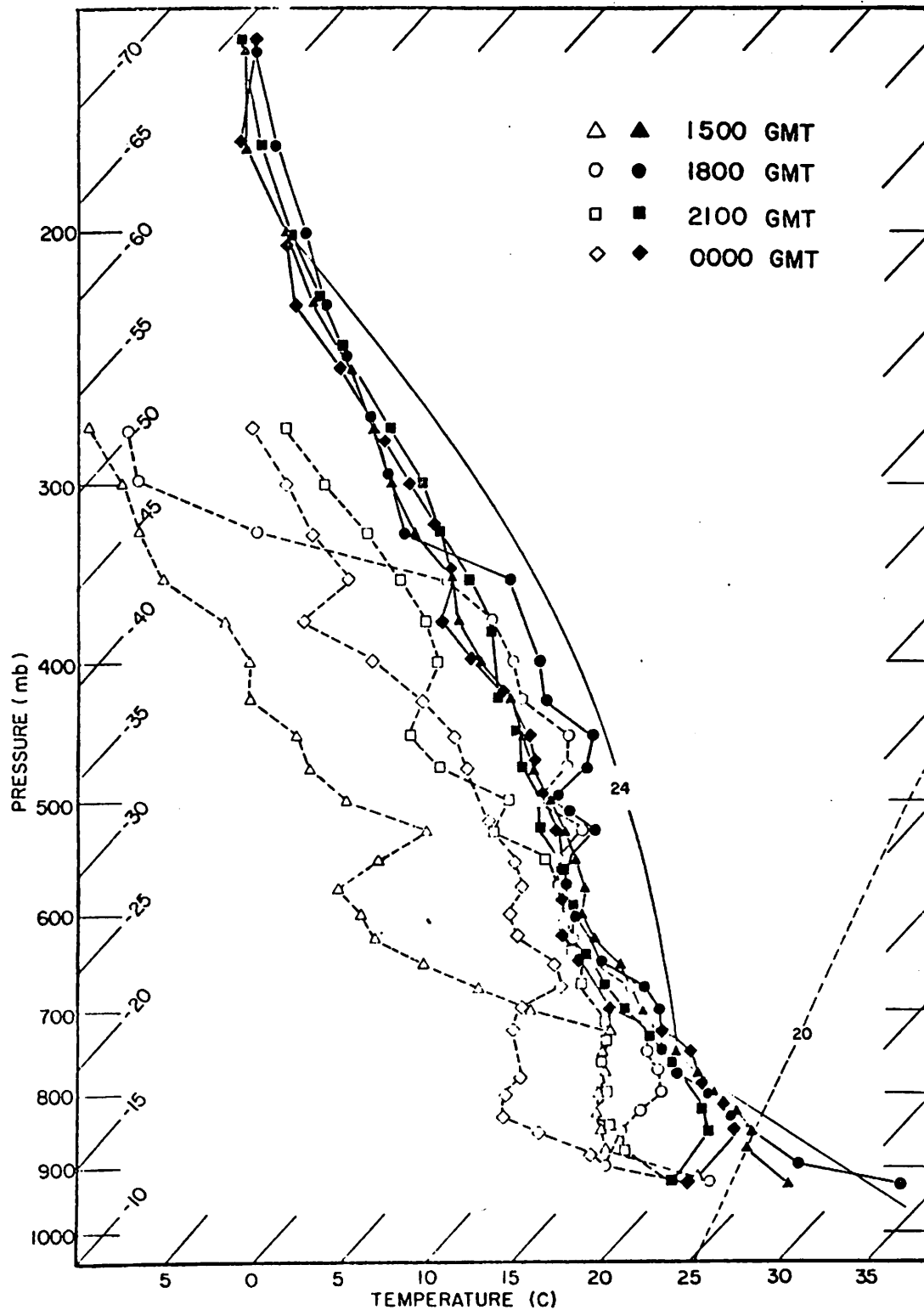


Figure 2-11 Atmospheric soundings taken at Big Spring on 8 July 1977. Open symbols connected by dashed lines are dew-point and full symbols connected by solid lines are temperature on a skew T-log P chart.

fronts. The soundings showed that the atmosphere was almost saturated and there was a large positive area for free convection at 1800 GMT when the thunderstorms developed. The diamond shape found in the sounding at 2100 GMT enlarged by 0000 GMT 9 July, and could be associated with the dissipating stages of the thunderstorms.

The comparisons made in this study demonstrate the consistency of results derived from satellite radiance measurements with analyses of radar and raingage data, thereby establishing the usefulness of satellite data in the absence of radar or raingage measurements.

A number of factors indicated that convective activity should be expected on each of the four case study days. The K-index of stability was large enough to predict the likely occurrence of thunderstorms each day. Precipitable water values revealed at least average moisture on all four days, although the 22 June and 8 July totals were noticeably higher. The temperature soundings appeared to possess sufficient potential instability to support convective development if it were initiated by low-level instability. The critical element was found to be a forcing mechanism for the precipitation process. In the absence of forcing, vigorous convective activity did not develop within the target area on 24 or 27 June, although some cumulonimbus did advect in.

Further studies are planned to develop objective methods of estimating rainfall from satellite visible and infrared data. The estimated precipitation volumes could be verified by raingage measurements and digital radar reflectivity data. The rainfall volume estimated by satellite photographic imagery would also be helpful in comparison with those derived from the digital satellite radiance data. Once established, such a method could be applied to thunderstorms outside the raingage network to estimate rainfall volume. This is the long-term goal of the present study. With this development, it should be possible to extend the coverage of programs such as HIPLEX beyond the range of radar and raingage measurements.

The present study has demonstrated the reliability of satellite radiance data when compared with radar and raingage measurements. However, the

problem of working with observations from three systems with such different spatial resolution was formidable. The superposition of patterns in this study was performed subjectively by hand. Techniques which utilize an objective computer-based approach are becoming available and should permit more ambitious efforts in the future.

### Task 3. Rainfall Analysis

As a part of this task, a computer program was developed to display the M-33 (Snyder) digitized radar data in the form of vertical cross sections (RHI's). This program, written in PL/I, uses edited radar data in DVIP units as input, and produces as printed output plots of every data value in units of dBZ. Hand analyses of these computer plots of data gave insight into the three-dimensional structure of the radar echoes. Output from this computer program proved useful in performing the analyses described under Task 2.

Analysis of the M-33 radar data, when integrated with satellite and rawinsonde data in a case study of 8 July 1977, showed strong similarities to radar precipitation patterns in mesoscale convective systems observed in the tropics, where digitized radar data have proven to be a useful tool in studies aimed at understanding the structure and behavior of mesoscale convective systems. In particular, quantitative radar data from the Global Atmospheric Research Program's Atlantic Tropical Experiment (GATE) have helped to establish the importance of mesoscale precipitating anvil clouds to the dynamics and thermodynamics of tropical cloud clusters (Houze, 1975, 1977; Leary and Houze, 1978, 1979 a,b). These anvil clouds have horizontal dimensions on the order of  $10^4$  km<sup>2</sup>, lifetimes of several hours or more, and extend from the middle troposphere (~700 mb) to the upper troposphere (~200 mb). Precipitation in and beneath anvil clouds exhibits a characteristic signature when observed by radar. Its striking horizontal uniformity over a widespread area and its long duration are a sharp contrast to the strong horizontal gradients and vertical orientation of the short-lived echo patterns that accompany convective cells. Frequently, a narrow horizontal layer of high reflectivity called the bright band is observed just below the 0°C isotherm when the radar scans a vertical cross section through horizontally uniform precipitation.

Only rarely has horizontally uniform precipitation accompanied by a radar bright band been reported in convective systems in middle latitudes (e.g., the squall-line system described by Zwack and Anderson (1970)). Yet recent studies of intense convective systems in middle latitudes (Sanders and Paine, 1975; Sanders and Emanuel, 1977; Ogura and Liou, 1979) have emphasized the presence and importance of mesoscale dynamical features in such systems. Ogura and Liou (1979), in their case study of a mid-latitude squall-line system, did note that as the peak rainfall rate diminished, an area of lighter rain became more widely spread.

The investigation of a mesoscale convective system over the Texas South Plains was undertaken to determine to what extent its structure resembles that of tropical mesoscale systems, whose precipitation patterns show clear evidence for the presence of mesoscale dynamical features. The particular system chosen for study was a non-squall mesoscale convective system associated with a cold front. Less intense and less well-organized than a squall-line system, this case is more typical of mesoscale convective systems that produce the major summer precipitation events in this semi-arid region.

The data presented here were collected over the Texas South Plains on 8 July 1977 as part of the High Plains Cooperative Program (HIPLEX) sponsored by the Water and Power Resources Service's Office of Atmospheric Resources Management and the Texas Department of Water Resources. Digitized radar data were collected using the 9.1 cm M-33 radar operated by Meteorology Research, Inc., at Snyder. Table 3-1 lists the characteristics of this radar.

Table 3-1

HIPLEX RADAR CHARACTERISTICS SNYDER, TEXAS 1977	
Wavelength (cm)	9.1
Peak power (kW)	850
Beamwidth (deg)	1.6
Range bin size (km)	0.45
Azimuth recording increment (deg)	1

Rawinsonde data were collected at 3-hour intervals on 8 July at four stations.

Texas A&M University operated three of these, and the fourth, at Midland, was operated by the National Weather Service. In addition to hourly surface observations at Midland, ten special surface stations, provided by Meteorology Research, Inc., recorded temperature, relative humidity, pressure, wind speed and wind direction continuously. Scoggins (1977) has tabulated and described the processing of the rawinsonde and surface data. A dense network of rain gages was maintained by the Colorado River Municipal Water District. Both infrared and visible satellite imagery were obtained from the Geostationary Operational Environmental Satellite (GOES EAST). Surface and upper level synoptic data and analyses from the National Meteorological Center were also used for the research described in this paper.

### Larger Scales of Motion

Fig. 3-1 shows the enhanced infrared satellite imagery observed at 2100 GMT on 8 July 1977. The band of cloudiness extending from southwest to northeast across western Texas is located just behind a cold front at the surface which was moving southeastward in this area at about  $6.5 \text{ m s}^{-1}$ . This cold front was a large-scale feature, and extended northeastward to a low pressure center located in New York at 2100 GMT. The synoptic-scale surface flow was from the south and southeast ahead of the front, and from the northeast to the rear of the front. In the upper troposphere, the synoptic-scale flow at 300 mb over the Texas South Plains was southeasterly ahead (southeast) of the cloud band in Fig. 3-1, and southwesterly to the rear (northwest) of the cloud band. Winds at this level were light ( $\sim 5 - 10 \text{ m s}^{-1}$ ).

The mesoscale convective system described in this paper was, at 2100 GMT (1600 CDT), located within range of the radar at Snyder (black circle in Fig. 3-1). The enhanced satellite imagery in Fig. 3-1 shows that the coldest (highest) cloud tops associated with the cloud band over Texas lie in this area.

### The Mesoscale Precipitating Anvil Cloud

The mesoscale precipitation feature associated with the deep clouds over the Snyder radar in Fig. 3-1 had a lifetime of about 8 h, from 1640 GMT

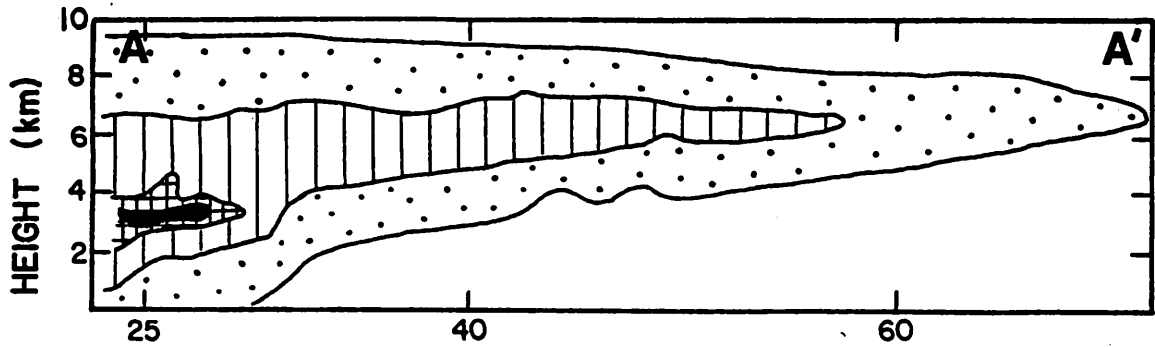


Fig.3-1. GOES EAST enhanced infrared satellite photograph of the cloud pattern over the Texas HIPILEX area at 2100 GMT on 8 July 1977. The circle outlines the range of the M-33 radar at Snyder.

on July 8 to 0100 GMT on July 9. From its first appearance as a pair of lines of small echoes oriented from northeast to southwest at a location about 50 km southeast of Snyder, the precipitation feature as a whole showed little motion, although it broadened considerably towards the northwest and southeast, as well as lengthened to the northeast and southwest. Fig. 3 - 2 shows the low-level precipitating pattern and an RHI along the azimuth of  $3^{\circ}$  observed by the radar at 2104 GMT, about midway through the feature's life cycle. At this time the low level echo coverage was approximately the maximum for the precipitation feature's lifetime. The vertical cross section in Fig. 3-2a shows that an extensive anvil of precipitation particles aloft extended to the rear of the precipitation feature at this time. Fig. 3-2a also shows that a distinct bright band of high reflectivity values was present in the portion of the anvil where precipitation reached the surface. The anvil of precipitation particles aloft was quite extensive. The heavy dashed line in Fig. 3-2b outlines its maximum extent. This mesoscale feature shows a strong resemblance to those observed in tropical cloud clusters (Houze, 1975, 1977; Leary and Houze, 1978, 1979 a,b), with its prominent bright band and horizontally oriented contours of reflectivity.

A 2100 GMT sounding at Post (see Fig. 3-2b), located near the outer boundary of the portion of the anvil containing precipitation-sized particles, shows further evidence of similarity with mesoscale precipitation systems observed over the tropical ocean. The lower portion of the sounding is shown in Fig. 3-3. In Fig. 3-4, the sounding is superposed on a collection of soundings compiled by Zipser (1977) to depict the thermodynamic structure of precipitating anvil clouds in the tropics, particularly those observed during GATE. In the layer between 600 and 900 mb, the 2100 GMT sounding at Post shows a strong similarity to tropical soundings beneath anvil clouds, suggesting that the mesoscale subsidence due to evaporative cooling that produces such soundings (Zipser, 1969, 1977; Brown, 1979) is also present in this case. The surface temperature at Post is consistent with its position outside the area where precipitation reached the surface.

The wind field in the vicinity of the mesoscale precipitation feature at 2100 GMT also shows similarities to tropical convective systems possessing mesoscale subsidence beneath anvil clouds. Fig. 3-5 shows the surface wind field at 2100 in the vicinity of the convective system. The wind flow is strongly diffluent, and the increase in wind speed downwind makes the



(a) DISTANCE FROM SNYDER RADAR (km)

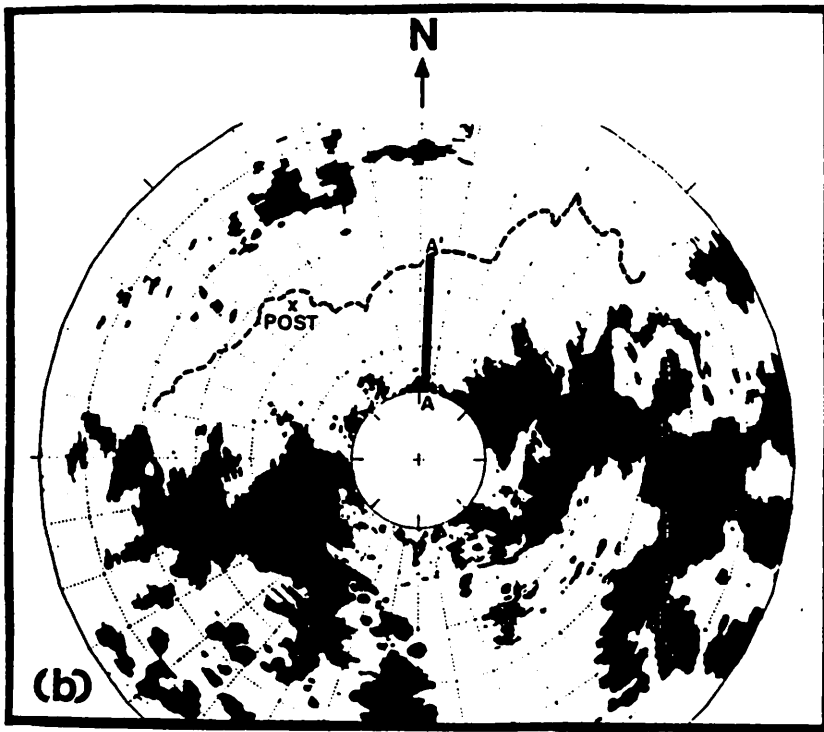


Fig.3-2. RHI (a) and low-level (1°) PPI (b) displays derived from Snyder digital radar data for 2104 GMT, 8 July 1977. RHI lies along line A-A' shown in PPI. Outside contour on RHI is boundary of weakest detectable echo, and inside contours are for 25, 30, and 35 dBZ. Echo boundary on PPI is 25 dBZ. Range marks on PPI are at 25, 40, 60, 80, 100, 120, and 130 km. The heavy dashed line on PPI outlines the maximum horizontal extent of precipitation particles detectable by radar in the anvil cloud aloft.

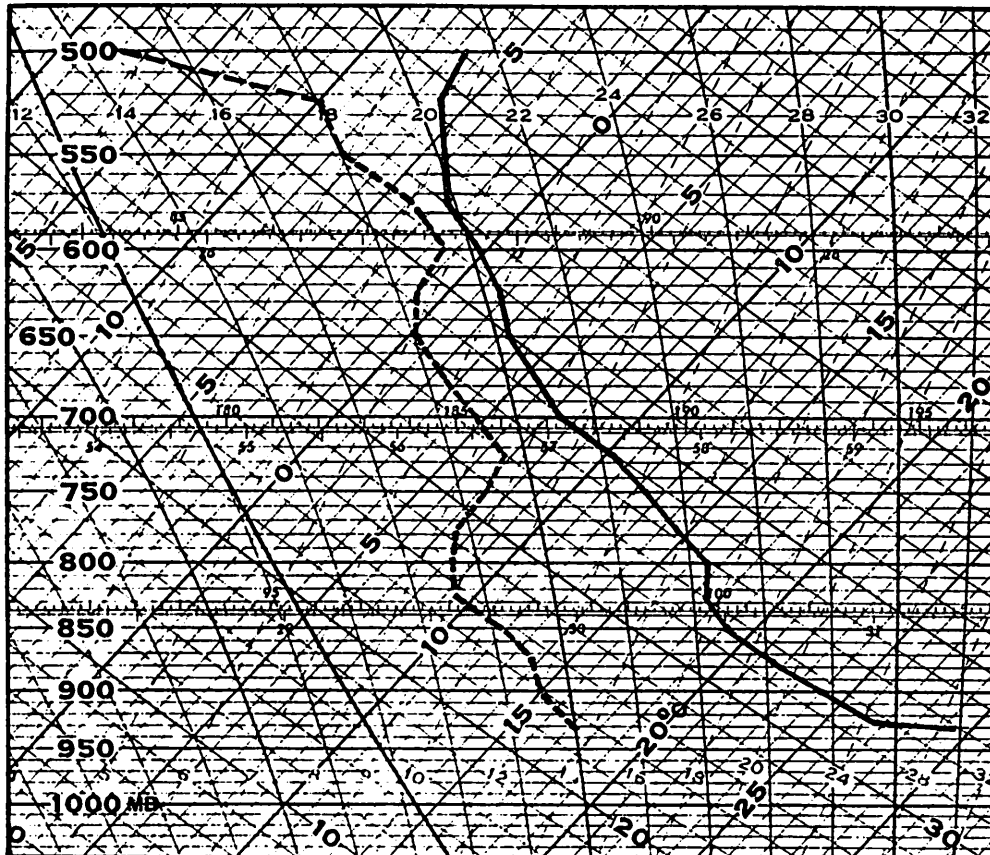


Fig.3-3 Temperature (solid line) and dew point (dashed line) at 2100 GMT on 8 July at Post plotted in skew T - log p format. Post is located at an elevation of 771 m above sea level.

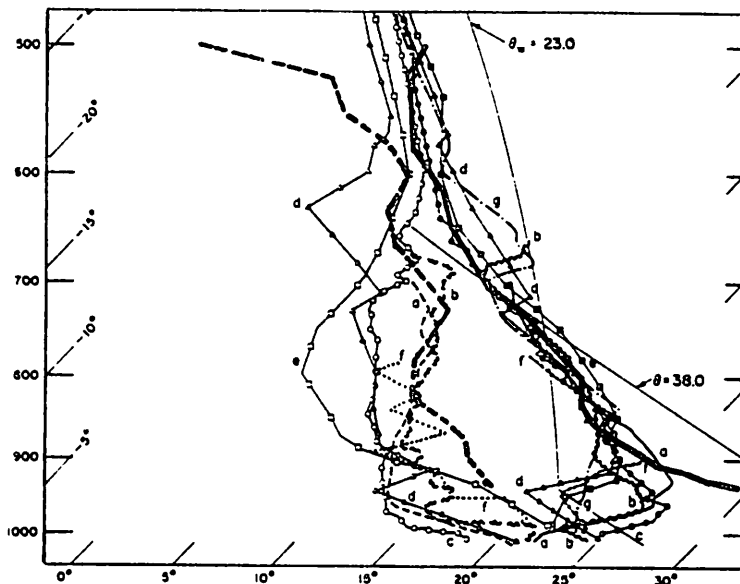


Fig.3-4 The 2100 GMT Post sounding from Fig.3-3 (heavy solid line is temperature, heavy dashed line is dew point) superposed on the lower portions of Zipser's (1977, Fig. 8) collection of soundings in and beneath tropical anvil clouds associated with intense tropical convection. The soundings are plotted in skew T - log p format.

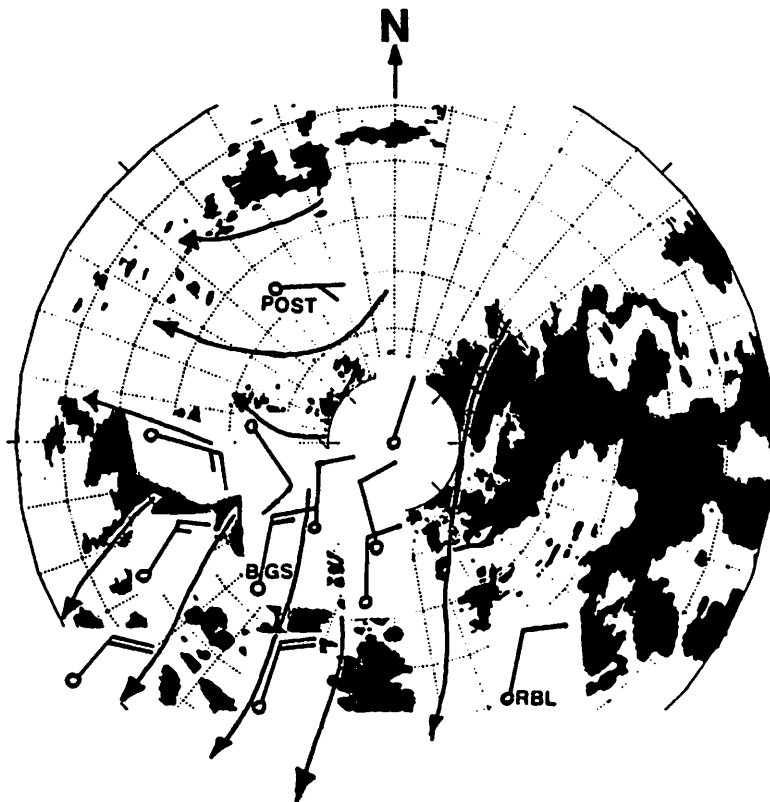


Fig.35 Surface winds at 2100 GMT on 8 July 1977 superposed on the low-level radar echo pattern of Fig.32b. A half-barb indicates  $2.5 \text{ m s}^{-1}$ , and a full barb indicates  $5 \text{ m s}^{-1}$ .

flow divergent as well. Such a wind field at the surface in the vicinity of precipitating anvil clouds has been noted by Zipser (1969, 1977).

Aloft, fewer wind observations were available. Table 3-2 lists wind observations at 25 mb intervals at 2100 GMT for one station (Post) at the rear edge of the anvil cloud as well as for one station in the precipitation area at the surface (Big Spring) and for one station in front of the precipitation feature (Robert Lee). Their positions are shown in Fig. 3-5. In the 350 to 250 mb (8-10 km) layer at Post, the relatively strong southerly winds are consistent with the northerly spread of the anvil cloud to the rear of the precipitation feature. (See Figs. 3-2a, b). Leary and Houze (1979 b) and Houze (1977) reported similar relationships between the orientation of the anvil and wind direction at upper levels. Comparing the strong southerly winds at Post between 350 and 250 mb with the weaker southeasterlies and easterlies at Big Spring and Robert Lee suggests divergence at upper levels associated with the anvil cloud. Again, a similar relationship has been reported for tropical cloud clusters by Houze (1977) and Leary (1979). They also observed convergence near the 700 mb level associated with anvil clouds. This too is suggested by the soundings in Table 2. In the layer between 750 and 500 mb (2-5 km) northerlies and easterlies at Post compare with southeasterlies and southerlies at the two southern stations. Convergence in this layer would provide mass continuity to account for subsidence beneath the anvil.

The precipitating anvil cloud associated with a mesoscale convective system over the Texas South Plains resembles anvil clouds observed over the tropical ocean in its radar echo pattern, including a bright band just below the 0°C isotherm (3.7 km), its thermodynamic structure indicative of mesoscale subsidence below 600 mb, and its wind field that suggests divergence near the surface, convergence in the vicinity of 700 mb, and divergence near 250 mb. To the extent that such resemblances exist, methods like those developed by Houze et. al. (1980) and Leary and Houze (1980) to compute vertical transports of mass and heat in tropical cloud clusters using digitized radar data may also be applicable to intense convective systems in middle latitudes.

Table 3-2  
WIND DIRECTION (DEGREES) AND SPEED ( $M S^{-1}$ ) AT 2100 GMT

LEVEL (MB)	POST	BIG SPRING (BGS)	ROBERT LEE (RBL)
850	084/6.6	054/7.4	091/3.8
825	048/3.3	053/6.0	138/6.3
800	347/3.0	035/4.6	149/6.6
775	347/1.9	357/0.8	143/7.9
750	025/2.4	200/2.0	147/7.3
725	045/2.1	168/1.6	145/5.8
700	073/1.6	158/1.0	135/5.5
675	098/1.6	210/0.9	135/5.0
650	006/1.1	155/0.7	118/4.1
625	315/3.2	162/2.0	096/3.8
600	317/3.2	187/2.7	111/4.0
575	334/3.0	176/1.8	134/4.7
550	329/3.1	095/1.8	123/4.4
525	321/3.5	092/1.8	128/3.1
500	345/2.8	163/1.5	137/4.6
475	041/1.5	161/2.6	130/5.3
450	120/3.1	176/8.1	114/4.4
425	139/3.1	163/15.2	174/3.3
400	144/3.4	149/9.9	175/6.7
375	208/1.7	148/10.5	166/5.8
350	212/6.7	156/11.0	147/4.5
325	169/13.9	159/9.6	151/6.4
300	172/14.8	158/7.3	137/8.3
275	179/12.3	169/1.4	127/7.2
250	180/11.5	154/2.4	082/1.3
225	188/8.6	074/1.6	029/2.9
200	206/8.6	077/0.6	078/4.4

## Rainfall Network Data Processing and Analysis

The purpose of the rainfall analysis is two-fold; first to investigate the use of surface rainfall and rainfall-calibrated radar data as response variables in seeding evaluation, and second, to derive rainfall input to hydrologic models. In either case an effort is being made to define "natural variability" as it applies to storms in the Texas HIPLEX region.

Analysis of 1977 and 1978 field-season data has been completed. Isohyetal maps of surface rainfall patterns with 15-minute temporal resolution have been produced for each storm in which significant rainfall was collected by the raingage network. Rainfall intensity and duration, storm size and velocity and total integrated rainfall have been studied as a function of synoptic and sub-synoptic weather patterns. A technical report on Texas HIPLEX rainfall will be published at the completion of the 1979 data analysis.

Total water volume has been computed for selected rainfall periods by first constructing a network of triangles defined by the gage locations, computing the average rainfall over each triangle and summing over the entire network. The results of this analysis are shown in Tables 3-3 and 3-4 for 1977 and 1978 respectively. Note that total volume is expressed in both acre-feet and cubic meters.

Additional storm data is provided in Tables 3-5 and 3-6. In these tables, the storm period refers to the total time that rainfall was observed in the network and the storm movement reflects the average movement of the entire storm during the period. The individual storm units represent one or more cells which produced identifiable rainfall patterns at the surface. Maximum storm area is the largest area enclosed by the 0.1 inch isohyet.

For the storms analyzed, rainfall periods varied from 3 hours on 21 June 1977 to 6½ hours on 3 July 1978. This extended period of rainfall was associated with strong surface heating in a moist unstable air mass and resulted in the development of a large number of storm units (convective cells). Shorter periods were related to the passage of short waves at upper levels or air mass discontinuities at the surface.

Table 3-3 1977 Precipitation

<u>Date</u>	<u>Time Period (CDT)</u>	<u>Rainfall Volume</u>	
		<u>Acre-Feet</u>	<u>10<sup>6</sup> m<sup>3</sup></u>
21 June	0000-0015	7614	9.391
	0015-0030	7785	9.602
	0030-0045	7720	9.522
	0045-0100	8634	10.649
	0100-0115	8968	11.061
	0115-0130	8373	10.327
	0130-0145	8235	10.157
	0145-0200	5528	6.818
	0200-0215	5997	7.397
	0215-0230	5686	7.013
	0230-0245	2684	3.311
	0245-0300	1391	1.716
21 June	2245-2300	2291	2.826
	2300-2315	2673	3.297
	2315-2330	2158	2.662
	2330-2345	2004	2.472
	2345-0000	1767	2.179
22 June	0000-0015	758	0.935
	0015-0030	580	0.715
	0030-0045	476	0.587
	0045-0100	434	0.535
22 June	1300-1315	670	0.826
	1315-1330	908	1.120
	1330-1345	1746	2.154
	1345-1400	2550	3.145
	1400-1415	4122	5.084
	1415-1430	2311	2.850
	1430-1445	3652	4.504
	1445-1500	2381	2.937
	1500-1515	1359	1.676
	1515-1530		
	1530-1545		
	1545-1600	2844	3.508
	1600-1615	5262	6.490
	1615-1630	2831	3.492
	1630-1645	2387	2.944
	1645-1700	4100	5.057
	1700-1715	3631	4.479
1715-1730	2633	3.248	
1730-1745	3065	3.780	

Table 3-3 (cont.)

<u>Date</u>	<u>Time Period (CDT)</u>	<u>Rainfall Volume</u>	
		<u>Acre-Feet</u>	<u>10<sup>6</sup> m<sup>3</sup></u>
23 June	0415-0430	951	1.173
	0430-0445	565	0.697
	0445-0500	1031	1.272
	0500-0515	835	1.030
	0515-0530	592	0.730
	0530-0545	315	0.389
	0545-0600	441	0.544
23 June	1500-1515	3078	3.796
	1515-1530	2462	3.037
	1530-1545	2549	3.144
	1545-1600	2391	2.949
	1600-1615	1299	1.602
	1615-1630	647	0.798
	1630-1645	1606	1.981
	1645-1700	3395	4.187
	1700-1715	2707	3.339
	1715-1730	1712	2.112
	1730-1745	1250	1.542
	1745-1800	2233	2.754
	1800-1815	1671	2.061
	1815-1830	1374	1.695
8 July	1330-1345	4046	4.990
	1345-1400	5004	6.172
	1400-1415	4574	5.642
	1415-1430	5727	7.064
	1430-1445	8875	10.947
	1445-1500	9268	11.431
	1500-1515	5871	7.241
	1515-1530	6198	7.645
	1530-1545	4046	4.990
	1545-1600	1919	2.367
	1600-1615	1184	1.460
	1615-1630	926	1.142
	1630-1645	1033	1.274
	1645-1700	1009	1.245

Table 3-4 1978 Precipitation

<u>Date</u>	<u>Time Period (CDT)</u>	<u>Rainfall Volume</u>	
		<u>Acre-Feet</u>	<u>10<sup>6</sup> m<sup>3</sup></u>
5 June	1700-1715	1905	2.350
	1715-1730	3618	4.463
	1730-1745	3772	4.652
	1745-1800	3158	3.895
	1800-1815	4544	5.605
	1815-1830	9203	11.351
	1830-1845	8498	10.482
	1845-1900	6343	7.824
	1900-1915	8957	11.048
	1915-1930	3978	4.907
	1930-1945	8599	10.606
	1945-2000	7090	8.745
	2000-2015	3988	4.919
	2015-2030	855	1.055
	2030-2045	687	0.847
6 June	0830-0845	186	0.229
	0845-0900	522	0.644
	0900-0915	826	1.019
	0915-0930	2173	2.680
	0930-0956	5216	6.434
	0945-1000	5671	6.995
	100-1015	4864	5.999
	1015-1030	3774	4.655
	1030-1045	3149	3.884
	1045-1100	2144	2.644
	1100-1115	1538	1.897
	1115-1130	1242	1.532
	1130-1145	1554	1.917
	1145-1200	1581	1.950
	1200-1215	1138	1.404
	1215-1230	850	1.048
	130-1245	790	0.974
1245-0100	475	0.586	
0100-0115	257	0.317	
3 July	1700-1715	1246	1.537
	1715-1730	3236	3.991
	1730-1745	2453	3.026
	1745-1800	2390	2.948
	1800-1815	2067	2.549
	1815-1830	3427	4.227
	1830-1845	4872	6.009
	1845-1900	3808	4.697
	1900-1915	2853	3.519
	1915-1930	4513	5.566
	1930-1945	3656	4.509
	1945-2000	3092	3.814

Table 3-4 (cont.)

<u>Date</u>	<u>Time Period (CDT)</u>	<u>Rainfall Volume</u>	
		<u>Acre-Feet</u>	<u>10<sup>6</sup> m<sup>3</sup></u>
3 July (cont.)	2000-2015	3002	3.703
	2015-2030	1807	2.229
	2030-2045	1678	2.070
	2045-2100	2315	2.855
	2100-2115	2325	2.868
	2115-2130	920	1.135
	2130-2145	1273	1.570
	2145-2200	1078	1.330
	2200-2215	1593	1.965
	2215-2230	1297	1.600
	2230-2245	1219	1.504
	2245-2300	1268	1.564
	2300-2315	994	1.226
	2315-2330	345	0.426
	2330-2345	534	0.659
	2345-0000	701	0.865
22 July	1415-1430	166	0.205
	1430-1445	427	0.527
	1445-1500	492	0.607
	1500-1515	897	1.106
	1515-1530	653	0.805
	1530-1545	1174	1.448
	1545-1600	3158	3.895
	1600-1615	3051	3.763
	1615-1630	2154	2.657
	1630-1645	2253	2.779
	1645-1700	3295	4.064
	1700-1715	3046	3.757
	1715-1730	832	1.026
	1730-1745	282	0.348
	1745-1800	115	0.142
1800-1815	207	0.255	
1815-1830	136	0.168	
23 July	1500-1515	2806	3.461
	1515-1530	2387	2.944
	1530-1545	2531	3.122
	1545-1600	2737	3.376
	1600-1615	5622	6.934
	1615-1630	6153	7.589
	1630-1645	5317	6.558
	1645-1700	4288	5.289
	1700-1715	3097	3.820
	1715-1730	1866	2.302
	1730-1745	1432	1.766
	1745-1800	1403	1.731
	1800-1815	958	1.182
	1815-1830	739	0.912
	1830-1845	517	0.638
1845-1900	535	0.660	

Table 3-5 1977 Storm Data

DATE	PERIOD (hrs)	MOVEMENT		INDIVIDUAL STORM UNITS			
		(km/hr)	(deg)	Unit	Lifetime (hrs)	Max. Area (km <sup>2</sup> )	Max. Intensity (in/hr)
21 June 77	3.00	32	320	A	2.75	2680	2.2
				B	0.50	375	0.8
				C	0.25	1219	1.4
				D	0.75	760	1.2
				E	1.50	700	1.9
				F	0.75	405	1.7
				G	0.50	250	0.6
22 June 77	4.25	24	300	A	2.50	920	1.0
				B	0.75	195	2.1
				C	0.50	800	2.1
				D	0.75	276	0.5
				E	1.75	560	1.6
				F	2.00	1140	2.2
				G	1.00	1554	1.5
23 June 77	3.50	10	110	A	2.00	810	3.0
				B	2.00	624	2.6
8 July 77	3.50	30	165	A	3.00	966	3.4
				B	0.75	136	1.9
				C	2.25	760	2.3
				D	0.75	380	1.5
				E	0.50	440	2.5
				F	0.75	252	1.2
				G	0.50	437	0.2

Table 3-6 1978 Storm Data

DATE	PERIOD (hrs)	MOVEMENT		INDIVIDUAL STORM UNITS			
		(km/hr)	(deg)	Unit	Lifetime (hrs)	Max. Area (km <sup>2</sup> )	Max. Intensity (in/hr)
5 June 78	3.75	16	280	A	2.25	1290	5.6
				B	0.25	260	1.2
				C	0.75	500	1.7
				D	2.25	1760	3.6
				E	0.75	805	0.5
3 July 78	6.50	32	290	A	1.50	504	1.1
				B	0.50	320	0.6
				C	0.50	208	0.6
				D	2.50	300	1.7
				E	0.50	476	0.4
				F	1.50	855	1.6
				G	1.50	308	1.3
				H	1.25	1880	1.5
				I	0.50	264	1.3
				J	1.00	340	1.2
				K	2.00	440	1.4
				L	1.25	168	0.9
				M	1.50	858	0.4
22 July 78	4.25	14	290	A	0.50	144	0.6
				B	1.00	276	0.2
				C	0.75	340	0.4
				D	0.75	462	0.6
				E	1.25	312	1.1
				F	1.75	532	2.2
				G	1.50	187	1.7
				H	1.75	576	2.0

Table 3-6 1978 Storm Data (cont.)

DATA	PERIOD (hrs)	MOVEMENT		Unit	INDIVIDUAL STORM UNITS		
		(km/hr)	(deg)		Lifetime (hrs)	Max. Area (km <sup>2</sup> )	Max. Intensity (in/hr)
23 July 78	4.00	16	270	A	4.00	1178	3.7
				B	1.50	320	1.4
				C	1.75	225	1.8
				D	0.75	759	3.7
				E	0.75	308	1.5

Note that rainfall intensities, based on 15-minute data resolution, ranged from less than 0.5 inches per hour to more than 5.5 inches per hour in the heaviest storm. A storm classification system based upon rainfall intensity, storm duration, rainfall volume, time between events and meso-synoptic weather type is being developed as a first step in generating long periods of precipitation for input to hydrological models.

Rainfall data collected during the 1979 field season have been processed in a manner acceptable to the Water and Power Resources Service and forwarded to Denver for archival purposes.

#### Task 4. Radar Data Collection for the 1979 Field Experiment

On each day during the 1979 HIPLEX season when convective echoes were present, the SKYWATER radar was used to record digital radar. In addition, 16mm movies of the color television display were obtained to supplement the digital data collected on magnetic tape.

Table 4-1 lists the four scanning modes in which the digital radar data were recorded. The two aircraft modes were employed when HIPLEX cloud treatment missions were in progress. If the clouds to be treated were more than 50 km from the radar, the Aircraft Far Out mode was employed, while if the clouds to be treated were located within 50 km of the radar, data were recorded using the Aircraft Close In mode. When aircraft flew near cloud base to collect data for comparing radar reflectivity to rainfall rate, the Z/R mode was used. Data was recorded in the Monitoring mode when the HIPLEX aircraft were not engaged in a mission. Table 4-2 lists the times for which digital radar data was recorded in each of the four scanning modes. Table 4-3 lists the times for which 16 mm color photographs were obtained.

During aircraft operations, radar observations were made available whenever possible for guidance in the deployment of aircraft for cloud monitoring and treatment. Video tape recordings of the color television display, which showed the positions of HIPLEX aircraft made it possible to discuss aircraft operations during debriefings with reference to

Table 4-1

SKYWATER RADAR  
TEXAS HIPLEX SCANNING MODES  
1979

	Monitoring (MON)	Z/R (ZR)	Aircraft Far Out (ACF)	Aircraft Close In (ACC)
PRF	414	414	414	414
RANGE INTERVAL	1 Km	0.5 Km	0.5 Km	0.5 Km
RANGE DELAY	10 Km	10 Km	10 Km	10 Km
<u>A-SCAN</u>				
Samples	16	16	16	16
Elevation	1°	0.5°	1°	1°
<u>B-SCAN</u>				
Samples	16	32	8	8
Start	2°	1°	2°	2°
Stop	12°	3°	12°	20°
Steps	1°	0.5°	0.5°	1°
TIME INTERVAL	10 Min	5 Min	5 Min	5 Min

Table 4-2

## INVENTORY OF DIGITAL RADAR DATA

Calendar Date	Original Tape Label	A-file Name	Mode	Start Time (GMT)	End Time (GMT)
20 May 1979 /	T9140 A#	AT0140V	ACC	212641	220145
"	T9140 B#	"	ACC	220622	224530
"	T9140 C#	"	ACC	225256	2330
"	T9140 D#	"	ACC	233318	000743
"	T9141 A#	AT9141B	ACC	010021	011135
27 May 1979*	T9147 A	AT9147P	MON	154420	172820
"	T9147 B	"	MON	173417	192834
"	T9147 C	"	MON	193414	212910
"	T9147 D	"	MON	213413	232842
"	T9147 E	"	MON	233415	011000
"	T9148 A	"	ACC	011128	014043
"	T9148 B	"	MON	014447	034930
"	T9148 C	"	MON	035510	042410
28 May 1979*	T9148 D	AT9148T	ACF	191732	194942
"	T9148 E	"	ACF	195333	202305
"	T9148 F	"	MON	202540	220940
31 May 1979	T9151 A	AT9151S	MON	181855	185436
"	T9151 B	"	ACC	185740	193152
"	T9151 C	"	ACC	193248	200158
"	T9151 D	"	ACC	200315	203226
"	T9151 E	"	MON	203636	223056
"	T9151 F	"	MON	223635	003056
"	T9152 A	"	MON	003217	021639
"	T9152 B	"	MON	021745	031341

# Indicates 16 mm movie of the color television display not available for the time period of this tape

\* Indicates a mesoscale day

/ Indicates a rapid scan day

Calendar Date	Original Tape Label	A-file Name	Mode	Start Time (GMT)	End Time (GMT)
1 June 1979*	T9152 C	AT9152P	MON	151902	170712
"	T9152 D	"	MON	171005	183322
"	T9152 E	AT9152S	MON	185558	204019
"	T9152 F	"	MON	204610	224019
"	T9152 G	"	MON	224558	003503
"	T9153 A	"	MON	003717	020131
2 June 1979	T9153 B	AT9153O	MON	140740	154201
"	T9153 C	"	MON	154740	173202
"	T9153 D	"	MON	173740	192201
"	T9153 E	"	MON	192740	212202
4 June 1979*	T9155 A	AT9155R	MON	172117	175538
"	T9155 B	"	ACC	175739	182649
"	T9155 C	"	ACC	182753	190202
"	T9155 D	"	ACC	190309	193643
"	T9155 E	"	ACC	193742	201151
"	T9155 F	"	ACC	201257	204206
"	T9155 G	"	MON	204427	213849
"	T9155 H	"	ACC	214126	220221
"	T9155 J	"	ACC	220520	223929
"	T9155 K	"	ACC	224030	230944
"	T9155 L	"	MON	231225	005654
"	T9156 A	"	MON	010000	024300

\* Indicates a mesoscale day

Calendar Date	Original Tape Label	A-file Name	Mode	Start Time (GMT)	End Time (GMT)
5 June 1979* /	T9156 B	AT9156T	MON	192900	201420
"	T9156 C	"	ACC	201604	205013
"	T9156 D	"	ACC	205116	210524
"	T9156 E	"	MON	210659	222512
"	T9156 F	"	ACC	222512	224921
"	T9156 G	"	ACF	225107	231540
"	T9156 H	"	MON	231743	010205
7 June 1979 /	T9158 A	AT9158U	MON	205300	223719
8 June 1979* /	T9159 A	AT91590	MON	141124	155545
"	T9159 B	"	MON	160124	174545
"	T9159 C	"	MON	175124	192555
"	T9159 D	"	MON	193728	212150
"	T9159 E	"	MON	212535	230955
"	T9159 F	"	MON	231418	005839
"	T9160 A	"	MON	005957	014500
"	T9160 B	"	MON	015204	025634
9 June 1979*	T9160 C	AT91600	MON	145115	163530
"	T9160 D	"	MON	164109	181830
21 June 1979*	T9172 A #	AT9172U	MON	203400	222821
"	T9172 B #	"	MON	223400	002822
23 June 1979	T9175 A	AT9175B	MON	013218	022640
"	T9175 B	AT9175E	MON	043806	051236

\* Indicates a mesoscale day

# Indicates 16 mm movie of the color television display not available for the time period of this tape

/ Indicates a rapid scan day

Calendar Date	Original Tape Label	A-file Name	Mode	Start Time (GMT)	End Time (GMT)
24 June 1979*	T9175 C	AT9175T	MON	195717	203140
"	T9175 D	"	MON	203801	222223
"	T9175 E	"	MON	222511	000934
"	T9176 A	"	MON	001053	002600
25 June 1979	T9176 B	AT9176Q	MON	163845	182306
"	T9176 C	"	MON	182522	192501
"	T9176 D	"	ACC	193823	200743
"	T9176 E	"	ACC	201309	204219
"	T9176 F	"	ACC	204646	211555
"	T9176 G	"	ACC	212155	215105
"	T9176 H	"	MON	215549	234009
"	T9176 J	"	MON	234212	012635
26 June 1979	T9177 A	AT91770	MON	145150	163609
"	T9177 B	"	MON	164200	181314
"	T9177 C	"	MON	182148	195130
"	T9177 D	"	ACF	195331	201804
"	T9177 E	"	MON	202120	215735
"	T9177 F	"	MON	220121	223551
2 July 1979*	T9184 A	AT9184D	MON	032150	050619
3 July 1979*	T9184 B	AT9184S	MON	182200	201631
"	T9184 C	"	MON	202356	220826
"	T9184 D	"	MON	221341	000610
"	T9185 A	"	MON	001111	002820
"	T9185 B	"	ACC	003424	010333
"	T9185 C	"	ACC	010852	013801
"	T9185 D	"	ACC	014235	021145
"	T9185 E	"	MON	021810	024234

\* Indicates a mesoscale day

Calendar Date	Original Tape Label	A-file Name	Mode	Start Time (GMT)	End Time (GMT)
4 July 1979*	T9185 F	AT9185S	MON	184337	202100
"	T9185 G	"	MON	202832	221812
"	T9185 H	"	MON	222959	235800
5 July 1979*	T9186 A	AT91600	MON	143501	161932
"	T9186 B	"	ACC	165119	172029
"	T9186 C	"	ACC	172509	175420
"	T9186 D	AT9186S	ACC	185314	192223
"	T9186 E	"	ACC	193029	195938
"	T9186 F	"	ACC	200437	203347
"	T9186 G	"	ACC	203901	210811
"	T9186 H	"	ACC	211316	214226
"	T9186 J	"	ACC	214815	222156
"	T9186 K	"	MON	223334	235910
"	T9187 A	AT9187C	MON	020348	025818
6 July 1979*	T9187 B	AT9187S	MON	182055	194031
"	T9187 C	AT9187U	MON	203428	221850
"	T9187 D	"	MON	222616	223240
"	T9187 E	"	MON	225321	003742
"	T9188 A	AT9188B	MON	014527	022200
7 July 1979*	T9188 B	AT91800	MON	145405	162827
"	T9188 C	"	MON	163410	181832
"	T9188 D	"	MON	182416	190837
"	T9188 E	AT9188W	MON	225421	232850
"	T9188 F	"	ZR	233856	010242

\* Indicates a mesoscale day

Calendar Date	Original Tape Label	A-file Name	Mode	Start Time (GMT)	End Time (GMT)
8 July 1979	T9189 A#	AT9189U	MON	203921	205340
"	T9189 B#	"	ACC	205929	212842
"	T9189 C#	"	ACC	213325	220235
"	T9189 D	AT9189X	ZR	232640	003222
"	T9190 A	"	MON	003700	022300
"	T9190 B	"	MON	023009	030430
9 July 1979	T9190 C	AT9190P	MON	153938	172800
"	T9190 D	AT9190V	ZR	210314	211154
"	T9190 E	"	ACC	211525	213550
"	T9190 F	"	ACC	214008	214931
"	T9190 G	"	ZR	215222	222107
"	T9190 H	"	MON	222428	000852
"	T9191 A	"	MON	002035	020456
"	T9191 B	"	MON	021050	034512
12 July 1979	T9193 A	AT9193Q	MON	163424	182846
"	T9193 B	"	MON	183341	201802
14 July 1979*	T9195 A	AT9195P	MON	152826	172247
"	T9195 B	"	MON	172842	185310

# Indicates 16 mm movie of the color television display not available for the time period of this tape

\* Indicates a mesoscale day

Calendar Date	Original Tape Label	A-file Name	Mode	Start Time (GMT)	End Time (GMT)
15 July 1979	T9196 A	AT9196U	MON	200853	210322
"	T9196 B	"	ACF	210903	213333
"	T9196 C	"	ACF	213753	220225
"	T9196 D	"	MON	220707	235129
"	T9196 E	"	MON	235628	014048
"	T9197 A	"	MON	014527	031948
"	T9197 B	"	MON	032429	035851
16 July 1979*	T9197 C	AT9197S	MON	182810	202231
"	T9197 D	"	MON	202842	222305
"	T9197 E	"	MON	223100	233528
"	T9197 F	"	ACF	234719	001152
"	T9198 A	"	MON	002309	005500
17 July 1979*/	T9198 B	AT91980	MON	144803	163223
"	T9198 C	"	MON	163731	182152
"	T9198 D	"	MON	182813	195233
"	T9198 E	"	ZR	200140	205019
"	T9198 F	"	ACC	205327	210800
"	T9198 G	"	ACC	211505	214406
"	T9198 H	"	ACC	214850	221758
"	T9198 J	"	MON	222233	000654
"	T9199 A	"	MON	001148	015610
"	T9199 B	"	MON	020139	025610

\* Indicates a mesoscale day  
/ Indicates a rapid scan day

Calendar Date	Original Tape Label	A-file Name	Mode	Start Time (GMT)	End Time (GMT)
18 July 1979*/	T9199 C	AT91990	MON	144837	164320
"	T9199 D	"	MON	165431	184853
"	T9199 E	"	MON	185500	204922
"	T9199 F	AT9199V	MON	212356	231816
"	T9199 G	"	MON	232337	011758
"	T9200 A	"	MON	012544	030005
19 July 1979	T9200 B	AT92000	MON	143359	161846
"	T9200 C	"	MON	162515	181935
"	T9200 D	"	MON	182752	202213
"	T9200 E	AT9200U	MON	205414	224836
"	T9200 F	"	MON	225426	004847
20 July 1979	T9201 A	AT92010	MON	145008	164437
"	T9201 B	"	MON	165008	171510

\* Indicates a mesoscale day  
/ Indicates a rapid scan day

Table 4-3

## INVENTORY OF 16MM MOVIE FILM

Reel Number	Julian Day	Start Time (GMT)	End Time (GMT)	Calendar Day
1	146	1422	1433	26 May
"	"	1912	2012	"
"	147	1534	2400	27 May
"	148	0000	0420	"
"	"	1916	2209	28 May
2	151	1840	2400	31 May
"	152	0000	0314	"
"	"	1419	2400	1 June
"	153	0000	0201	"
"	"	1408	2122	2 June
"	155	1721	2400	4 June
"	156	0000	0243	"
"	"	1855	2305	5 June
3	158	2124	2237	7 June
"	159	1350	2400	8 June
"	160	0000	0257	"
"	"	1350	1505	9 June
"	"	1522	1816	"
4	175	0132	0233	23 June
"	"	0438	0512	"
"	"	1947	2400	24 June
"	176	0000	0034	"
"	"	1639	2400	25 June
"	177	0000	0127	"
"	"	1444	2246	26 June

Reel Number	Julian Day	Start Time (GMT)	End Time (GMT)	Calendar Day
5	183	2137	2137	1 July
"	184	0314	0511	2 July
"	"	1806	2400	3 July
"	185	0000	0251	"
"	"	1844	2324	4 July
"	186	1435	2318	5 July
6	186	2333	2400	5 July
"	187	0204	0258	"
"	"	1820	2400	6 July
"	188	0000	0219	"
"	"	1453	1909	7 July
"	"	2254	2400	"
"	189	0000	0037	"
"	"	2322	2400	8 July
"	190	0000	0304	"
"	"	1539	1722	9 July
"	"	2103	2400	"
"	191	0000	0025	"
"	"	0114	0345	"
"	193	1634	2018	12 July
"	195	1524	1901	14 July
7	196	2012	2400	15 July
"	197	0000	0359	"
"	"	1828	0000	16 July
"	198	0023	0102	"
"	"	1447	0000	17 July
"	199	0000	0256	"
"	"	1449	2400	18 July
"	200	0000	0300	"
"	"	1434	2026	19 July

Reel Number	Julian Day	Start Time (GMT)	End Time (GMT)	Calendar Day
8	200	2054	2400	19 July
"	201	0000	0048	"
"	"	1450	1715	20 July

Table 4-4

## INVENTORY OF RADAR VIDEO TAPES

SUMMER 1979

Calendar Day	Tape Number	Julian Day	Start Time (GMT)	End Time (GMT)
May 27	1	148	005509	015732
May 31	2	152	144559	145601
June 4	3	155	153440	153536
June 4	3	155	152527	153145
May 28	3	148	153510	154045
June 4	4	155	193136	203344
June 5	5	156	222150	232300
June 8	6	159	215827	230128
June 8	7	159-60	230827	001100
June 25	8	176	144351	150944
June 25	9	176	195634	205905
June 25	10	176	210245	220531
June 26	11	177	200201	201400
July 19	12	200	144140	144455
July 2	12	184	032715	042623
July 3	13	184	214500	224811
July 3	14	185	003246	013526
July 3	15	185	014546	024600
July 4	16	185	210242	220720
July 5	17	186	165216	175505
July 5	18	186	201719	211947
July 7	19	188-89	234146	003830
July 9	20	190	212000	222255
July 15	21	196	211655	221830
July 15	22	197	003116	012449
July 15	22	197	022650	023547
July 16	23	197-98	225800	004405
July 17	24	198	204849	214940
July 17	25	160	145637	150540
July 17	25	198	145610	150600

Calendar Day	Tape Number	Julian Day	Start Time (GMT)	End Time (GMT)
July 17	25	199	000030	004345
July 18	26	199-200	231825	002126

changing echo patterns. Table 4-4 lists the times for which video tapes made during the field project were saved for later analysis.

Weekly calibration tapes were mailed to the Bureau. Digital data tapes were all mailed to the University of North Dakota where they were edited with little or no delay after they were received. Processing through the University of North Dakota's RADPROC programs has also been completed on all 172 tapes.

#### Task 5. Support to the Field Program

During the 1979 Texas HIPLEX field program, a Laserfax was supplied by the Water and Power Resources Service to provide around-the-clock real-time support for the field operations. Texas Tech was responsible for the collection of visible and infrared imagery and their interpretation regarding the formation, location and degree of development of convective clouds. The information was provided in support of forecasting for operational decisions, declaration of mesoscale operational days and deployment of aircraft. The availability of both the specialized equipment and a meteorologist trained in the interpretation of satellite imagery proved to be a real asset to the program. A particularly valuable contribution proved to be to the calling of a mesoscale operational day. The 30-minute time resolution GOES imagery provided the only current information, in addition to surface observations, available before the decision on a mesoscale day was required. Besides providing input to forecast decisions, the GOES imagery was incorporated into both the daily weather briefings and the aircraft mission debriefings. The perspective of prevailing synoptic processes provided through this effort was recognized as highly beneficial to the field program. In addition, an opaque projector was generously loaned to us for the duration of the project by Howard College. This permitted the satellite imagery to be more effectively displayed and discussed during the daily weather briefings.

## REFERENCES

- Brown, J.M., 1979: Mesoscale unsaturated downdrafts driven by rainfall evaporation: A numerical study. J. Atmos. Sci., 36, 313-338.
- Houze, R.A., Jr., 1975: Squall lines observed in the vicinity of the Researcher during Phase III of GATE. Preprints 16th Radar Meteorology Conf., Houston, Amer. Meteor. Soc., 206-209.
- \_\_\_\_\_, 1977: Structure and dynamics of a tropical squall-line system. Mon. Wea. Rev., 105, 1540-1567.
- \_\_\_\_\_, C.-P. Cheng, C.A. Leary, and J.F. Gamache, 1980: Cloud mass and heat fluxes over tropical oceans: Diagnosis from radar and synoptic data. J. Atmos. Sci., in press.
- Leary, C.A., 1979: Behavior of the wind field in the vicinity of a cloud cluster in the Intertropical Convergence Zone. J. Atmos. Sci., 36 631-639.
- \_\_\_\_\_, and R.A. Houze, Jr., 1978: Observations of horizontally uniform precipitation and radar bright bands in the tropics. Preprints 18th Conf. on Radar Meteorology, Atlanta, Amer. Meteor. Soc., 1-8.
- \_\_\_\_\_, and \_\_\_\_\_, 1979a: Melting and evaporation of hydrometeors in precipitation from the anvil clouds of deep tropical convection. J. Atmos. Sci., 36, 669-679.
- \_\_\_\_\_, and \_\_\_\_\_, 1979b: The structure and evolution of convection in a tropical convection. J. Atmos. Sci., 36, 437-457.
- \_\_\_\_\_, and \_\_\_\_\_, 1980: Cloud mass and heat fluxes over tropical oceans: The role of mesoscale motions in intense convective systems. J. Atmos. Sci., in press.
- Ogura, Y., and M.-T. Liou, 1979: The structure of a mid-latitude squall line: A case study. Submitted to J. Atmos. Sci.
- Sanders, F., and R.J. Paine, 1975: The structure and thermodynamics of an intense mesoscale convective storm in Oklahoma. J. Atmos. Sci., 32, 1563-1579.
- \_\_\_\_\_, and K.A. Emanuel, 1977: The momentum budget and temporal evolution of a mesoscale convective system. J. Atmos. Sci., 34, 322-330.
- Scoggins, J.R., 1977: Texas HIPLEX Mesoscale Experiment - Summer 1977 Data Tabulations. Final Report, TWDB Contract No. 14-70030. Available from Texas Department of Water Resources, Austin, Texas.

Zipser, E.J., 1969: The role of organized unsaturated convective downdrafts in the structure and rapid decay of an equatorial disturbance. J. Appl. Meteor., 8, 799-814.

\_\_\_\_\_, 1977: Mesoscale and convective scale downdrafts as distinct components of squall-line circulation. Mon. Wea. Rev., 105, 1568-1589.

Zwack, P., and C. Anderson, 1970: 25 July 1969: Showers and continuous precipitation. Preprints 14th Radar Meteorology Conf., Tucson, Amer. Meteor. Soc., 335-338.